Article

Cell Host & Microbe

Hadal topography incubates hidden microbial hotspots in the deepest ocean

Graphical abstract

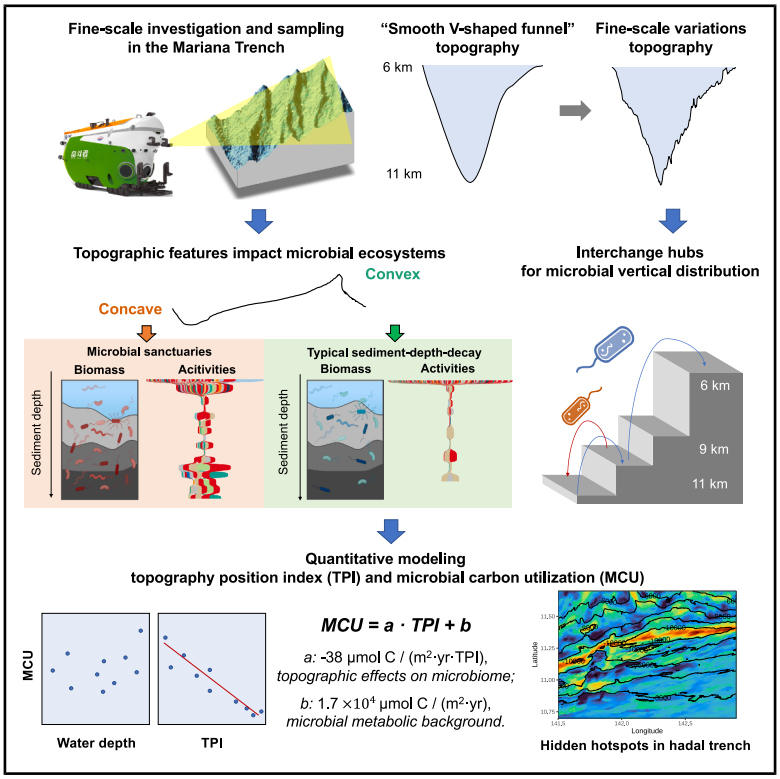

Highlights

- Topography is an overlooked determinant of heterogeneity in hadal microbiomes
- Trench bottoms act as refugia, preserving microbial biomass, diversity, and activity
- Fine-scale concave-convex topography shapes the microbiome at similar water depth
- Concave sites incubate hidden microbial hotspots and may relay upward dispersal

Authors

Weishu Zhao, Jing Wang, Chuanxu Chen, ..., Liang Dong, Yao Zhang, Xiang Xiao

Correspondence

zjxiao2018@sjtu.edu.cn

In brief

Zhao et al. apply integrated multi-omics, geochemical, and fine-scale topographic analyses of sediments across 55 locations in the Mariana Trench to reveal that hadal topography is an overlooked yet important determinant of microbial ecosystems and activities, with implications for understanding microbial hotspots and biogeochemical cycling in the deep ocean.

Zhao et al., 2026, Cell Host & Microbe *34*, 1523–1539
August 12, 2026
https://doi.org/10.1016/j.chom.2026.06.015

CellPress

Cell Host & Microbe

CellPress
OPEN ACCESS

Article

Hadal topography incubates hidden microbial hotspots in the deepest ocean

Weishu Zhao,[1,2,3,9] Jing Wang,[2,3,9] Chuanxu Chen,[4,9] Aijun Jiang,[1,2] Yinzhao Wang,[1] Aoran Hu,[1] Qi Qi,[1] Yunru Chen,[1] Weikang Sui,[5] Liang Dong,[5] Yao Zhang,[6] and Xiang Xiao[1,2,3,7,8,10,*]

[1]State Key Laboratory of Microbial Metabolism, International Center for Deep Life Investigation (IC-DLI), School of Life Sciences and Biotechnology, Shanghai Jiao Tong University, Shanghai 200240, China
[2]Yazhou Bay Institute of Deepsea Science and Technology, Hainan Research Institute, Shanghai Jiao Tong University, Sanya 572025, China
[3]Shanghai Changxing Ocean Laboratory, Shanghai Jiao Tong University, 1896 Changtao Road, Shanghai 201913, China
[4]Institute of Deep-Sea Science and Engineering, Chinese Academy of Sciences, Sanya 572000, China
[5]School of Oceanography, Shanghai Jiao Tong University, 1954 Huashan Rd., Shanghai 200030, China
[6]State Key Laboratory of Marine Environmental Science and College of Ocean and Earth Sciences, Xiamen University, Xiamen 361005, China
[7]Southern Marine Science and Engineering Guangdong Laboratory (Zhuhai), Zhuhai 510275, Guangdong, China
[8]Shanghai Academy of Natural Sciences (SANS), Shanghai, China
[9]These authors contributed equally
[10]Lead contact
*Correspondence: zjxiao2018@sjtu.edu.cn
https://doi.org/10.1016/j.chom.2026.06.015

SUMMARY

Plate subduction creates unique topographic features in hadal trenches, yet their influence on microbial ecosystems and the global ocean remains unclear. Here, we conducted a topography-targeted investigation across 6–11 km of water depth within the Mariana Trench, integrating metagenomic, metaproteomic, and geochemical analyses. Coupled with high-resolution topographic mapping, our analyses reveal topography as an overlooked determinant of hadal geochemical and microbial heterogeneity. Convex areas exhibit classical sediment-depth-decay patterns with sparse, cooperative microbial communities. Conversely, concave features maintain higher biomass and activity as well as dense microbial interactions. Critically, slope concave sites incubate previously unrecognized microbial hotspots and may serve as interchange hubs, potentially facilitating genetic exchange and upward dispersal of microorganisms from Earth's deepest regions to the broader ocean. Our findings demonstrate that topographic features, rather than water depth, significantly correlate with organic carbon influx and its microbial turnover rates, enabling predictive modeling of hadal carbon cycling with global implications.

INTRODUCTION

Hadal zones, representing ocean regions with water depth exceeding 6 km below sea level (b.s.l.), constitute the deepest places of Earth's solid surface.[1–3] Despite covering less than 1% of the global ocean area, hadal zones encompass 45% of the ocean's total depth range and consist primarily of 37 hadal trenches located at convergent tectonic plate boundaries, extending down to 11 km b.s.l. at the Challenger Deep in the Mariana Trench.[1–3] These trenches were formed through plate subduction, where the older, colder, and denser oceanic plates descend into the mantle while the lighter landward plates rise upward.[2] This subduction process creates complex multi-scale topographic complexity through oceanic plate bending and disruption by normal faults.[4–7] The resulting geological landscapes of faulting zones form horst and graben structures extending up to 120 km seaward off trench axes, with dip angles ranging from 10° to 40° that offset the seafloor by up to 1.2 km.[8] This topographic complexity distinguishes hadal trenches from other marine environments.

Hadal trenches serve as major organic matter depocenters in the ocean systems, where microbially mediated processes dominate biogeochemical turnover.[9,10] The long and narrow V-shaped morphology of trenches creates natural "funnels" that focus particulate organic matter from surrounding regions toward trench bottoms.[11] Seismic activities in trench regions trigger frequent earthquakes and mass-wasting events,[12,13] enhancing lateral transport and episodic organic matter delivery, thus amplifying the "funneling effect" of hadal trenches. This focusing of organic matter increases food availability for both hadal fauna and microorganisms, accelerating organic carbon degradation in hadal trenches.[1] Previous studies, using oxygen consumption rates as indicators, have shown that benthic microbial activity is generally 2–5 times higher along trench bottoms than in nearby abyssal settings with water depths shallower than 6 km b.s.l.[10,14,15] The interplay between intensified organic

carbon deposition and enhanced microbial utilization in hadal trenches plays a crucial role in regulating the deep-sea carbon cycle.[10,11]

Most hadal microbiological studies have focused on water depth as the primary controlling factor, since water depth represents the most characteristic environmental feature of hadal trenches, driving investigations toward broad-scale comparisons between trench bottoms (>10 km b.s.l.) and slopes (7–9 km b.s.l.)[16,17] or between hadal (>6 km b.s.l.) and non-hadal (<6 km b.s.l.) environments.[16,18] Some microbial indices have been suggested to correlate with water depth[11,14,17,19]; however, recent hadal investigations have found substantial heterogeneity in microbial communities among nearby locations at similar water depths.[20] Similarly, microbial activities vary by 2- to 3-fold along trench bottom samples within the same trench system.[10] These observations indicate that water depth alone cannot fully explain the spatial patterns of hadal microbial ecosystems. This unexplained heterogeneity points to the need for alternative environmental proxies beyond water depth.

Beyond water depth, we hypothesize that topographic features represent an overlooked determinant of hadal microbial community assemblages, their activities, and their mediated biogeochemical processes, creating spatial mosaics that cannot be predicted from water depth alone. Topographic features such as ridges and valleys directly influence local sedimentation patterns, organic matter accumulation, redox conditions, and hydrodynamic disturbances exposure.[1,8,21] As an integrative proxy for these multiple environmental factors, topography offers a scalable approach to understanding benthic microbial ecosystem variation.

However, testing this hypothesis requires investigating fine-scale topographic effects on hadal microbial ecosystems through high-precision sampling coupled with detailed topographic characterization, which is technically challenging under the extreme conditions of great depths and high pressures (60–115 MPa).[22] Conventional hadal sampling methods, such as gravity cores, multicore samplers, and free-fall landers, lack sufficient positioning precision.[22] While human-occupied vehicles (HOVs) provide precise positioning and sampling capabilities, topographic-targeted investigations in hadal environments have remained unexplored. Collectively, despite recognition of hadal topographic complexity, the lack of fine-scale investigations has left significant knowledge gaps regarding topographic effects on hadal microbial ecosystems, biogeochemical cycling, and global ocean processes.

Here, we conducted a comprehensive topography-targeted investigation to address these knowledge gaps. Normal faults are the most representative topographic features in the interior of hadal trench systems, creating complex three-dimensional seafloor topography such as fault scarps, sediment basins, ridges, valleys, and terraces.[5,8] Using HOV with centimeter-level precision, we designed targeted dives to four representative normal fault zones that span distinct depth ranges—from the southern abyssal rim (~6 km b.s.l.), through the subduction slope (9–10 km b.s.l.), to the bottom of the Challenger Deep (~11 km b.s.l.). These fault-generated landscapes allowed us to investigate both large-scale topography (trench bottom vs. slope and abyss) and fine-scale variations (concave vs. convex areas) at similar water depths, revealing systematic topographic effects on hadal microbial ecosystems. We integrated multi-omics analysis (metagenomic and metaproteomic) with extensive microbial biomass quantification and geochemical profiling (Figures 1A and 1B), which enabled accurate coupling of fine-scale topographic features with microbial ecosystems in the hadal environment. To achieve comprehensive spatial coverage across diverse topographic settings, we also incorporated metagenomic data from 86 sediment cores at 55 locations throughout the Mariana Trench, providing sufficient statistical power to identify systematic patterns of topographic effects on hadal microbial communities. Using these comprehensive data, we constructed an integrated topography-geochemistry-microbiology model, estimating hadal carbon cycling rates and providing insight into how topography shapes microbial ecosystems in Earth's deepest environments and their connections to the broader ocean.

RESULTS

Topography-targeted sampling captures microbial biomass and activity gradients across the Mariana Trench

During the cruise TS21-2 onboard research vessel (R/V) "Tan Suo Yi Hao," we used multibeam sonar to obtain the high-resolution bathymetric maps (resolution 110 m) of normal faults from the trench bottom to the southern rim along the subduction slope of the Mariana Trench (Figure 1A). These faults extended parallel to the trench axis (primarily east-west oriented), with horizontal lengths of 10–80 km and widths of several kilometers, creating both large-scale and fine-scale concave-convex topographic variations, especially on the southern slope (Figures 1B and 1C).

To investigate topographic influences on hadal microbial ecosystems, we conducted four topography-targeted dives using HOV *Fendouzhe* to sample representative fault zones across a depth gradient: the trench bottom of the Challenger Deep (FDZ070, 10,792–10,890 m b.s.l.), the subduction slope (FDZ069, 8,894–9,071 m b.s.l.; FDZ072, 9,218–9,580 m b.s.l.), and the southern abyssal rim (FDZ074, 5,882–5,922 m b.s.l.) (Figures 1A–1C). The HOV's 6-h benthic operating time and centimeter-level sampling precision enabled systematic collection of sediments from diverse topographic features within and across neighboring fault zones (Figures 1B and 1C). From 11 stations across these four dives, we obtained sediment geochemical profiles and metagenomic data, with four representative stations additionally yielding 16S rRNA gene quantification and metaproteomic data, enabling integrated multi-omics matching with fine-scale topographic parameters. In total, we collected 86 sediment cores from 55 distinct locations for subsequent analyses, including 25 cores from 11 locations during these topography-targeted dives, complemented by 61 additional cores from 44 locations across the Challenger Deep in the Mariana Trench (Figure 1A; Table S1).

At the four representative stations (FDZ070A, FDZ072A, FDZ072E, and FDZ074A), qPCR-based quantification of archaeal and bacterial 16S rRNA gene copy numbers revealed distinct biomass distribution patterns across depth zones (Figures 1D–1G) (STAR Methods). Slope and abyssal sites exhibited depth-dependent along sediment cores, declining from 10^7–10^8 copies/g at the surface (0–5 cm) to 10^2–10^5 copies/g

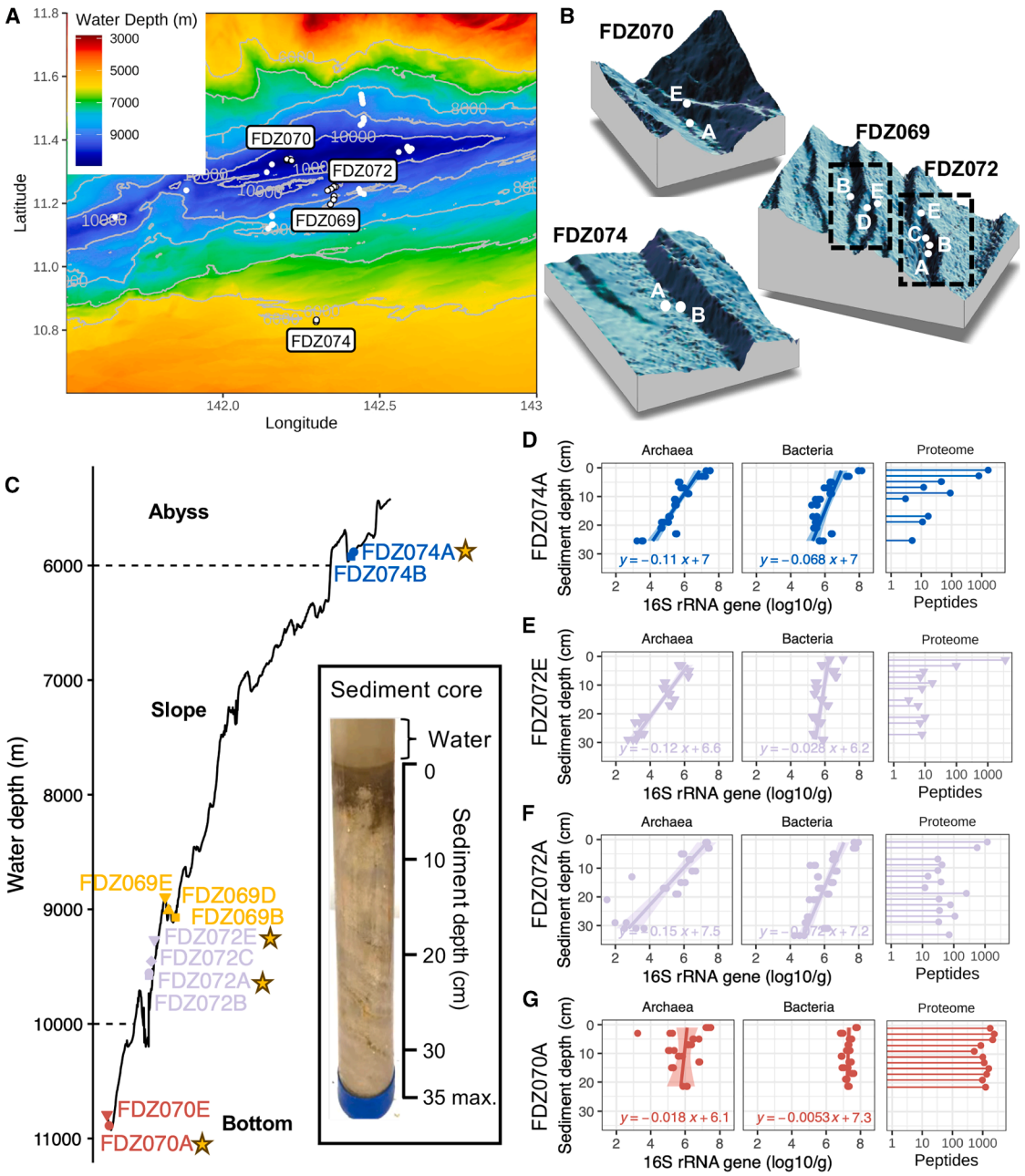

Figure 1. Geography, topography, and microbial biomass of representative normal faults in the Mariana Trench

(A) Bathymetric map of the sampling locations. White points indicate the locations of 86 sediment cores recovered from the Challenger Deep, Mariana Trench. Points with black strokes indicate samples recovered from the four topography-focused dives.

(B) Detailed 3D topography at the four focusing study areas, with letters indicating specific sampling locations.

(C) Schematic diagram illustrating the rugged terrain of the southern slope and the relative positions of sampling sites, alongside a photograph of a representative sediment push core. The push cores have a maximum capacity of 35 cm, with actual recovery lengths ranging from 14 to 35 cm depending on *in situ* sediment conditions.

(D–G) Sediment depth profiles of microbial biomass in four representative cores (indicated by stars in C): (D) abyssal site FDZ074A, (E) convex slope site FDZ072E, (F) concave slope site FDZ072A, and (G) trench axis site FDZ070A. The left and middle panels represent archaeal and bacterial 16S rRNA gene copy numbers, while the right panels indicate metaproteomic-identified unique peptides.

See also Tables S1 and S3.

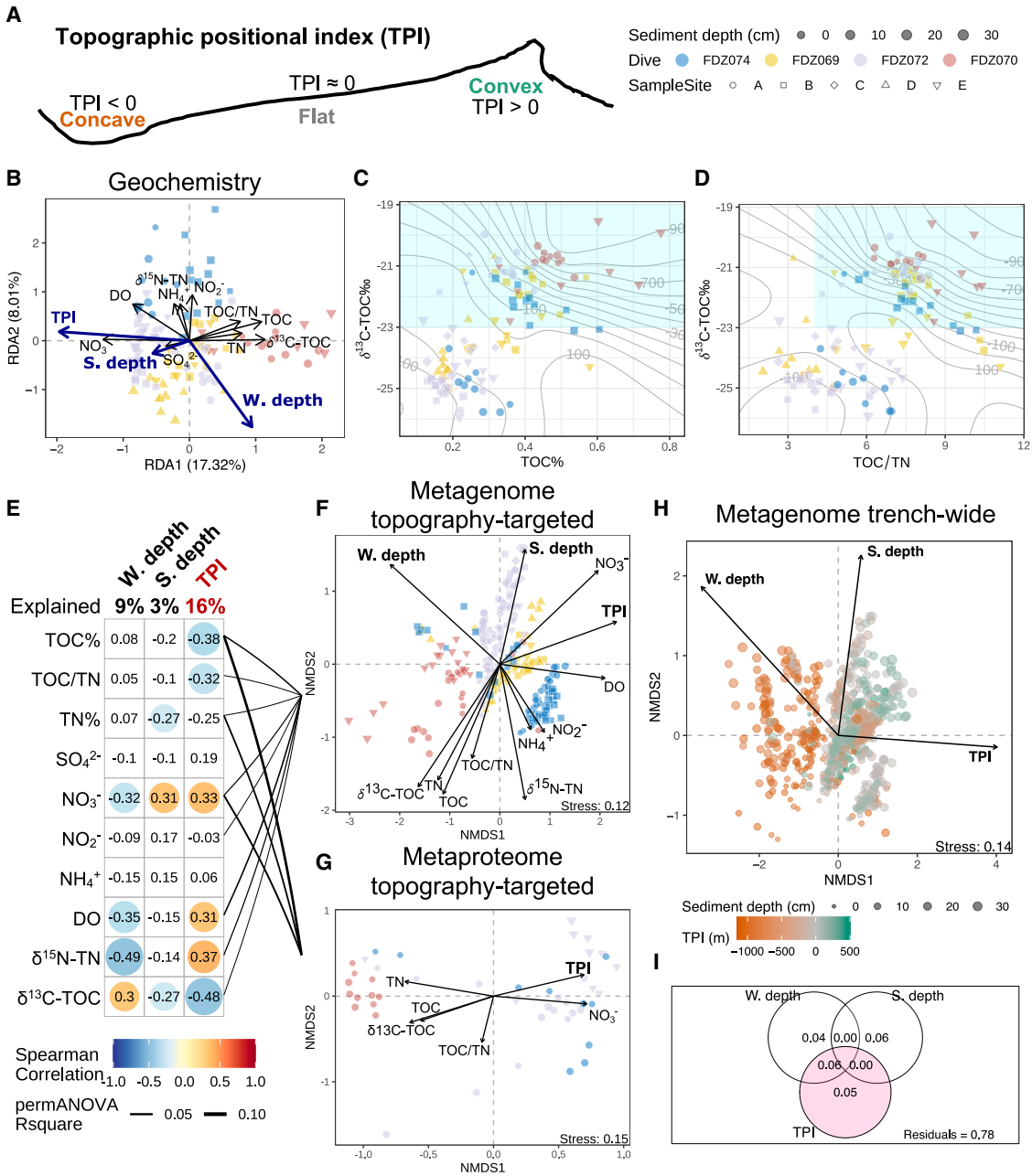

Figure 2. Topography as an overlooked determinant of geochemical and microbial heterogeneity

(A) Schematic diagram illustrating concave, flat, and convex positions defined by TPI.

(B) Redundancy analysis (RDA) of geochemical profiles across 11 stations from the four topography-targeted dives ($n = 116$). Thin arrows represent geochemical variables fitted into the ordination space; bold arrows indicate the three spatial factors: water depth, sediment depth, and TPI.

(C and D) Comparison of TOC content, its corresponding δ^{13}C-TOC values, and TOC/TN ratios with the reference range for typical oceanic organic carbon (cyan rectangle). TPI contour lines are fitted to illustrate the correspondence between topographic position and organic matter characteristics.

(E) Spearman correlation between the three spatial variables and sediment geochemistry. Significant correlations (FDR-adjusted $p < 0.01$) are highlighted by colored circles. Numbers at the top indicate the proportion of total geochemical variance explained by each spatial factor (adjusted R^2 from RDA). Lines connecting (E) to (F) and (G) denote significant correlations (permANOVA, $p < 0.01$) between geochemical variables and metagenomic or metaproteomic community structure, respectively.

(F) NMDS ordination of metagenome-based prokaryotic community dissimilarity (Bray-Curtis index) for topography-targeted samples ($n = 259$, from 11 stations). Arrows represent geochemical variables and spatial factors fitted into the ordination space.

(G) NMDS ordination of metaproteome-based active prokaryotic community dissimilarity from four representative sediment cores ($n = 47$, from 4 stations, corresponding to stations shown in Figures 1D–1G). Arrows represent geochemical variables and spatial factors fitted into the ordination space.

(legend continued on next page)

below 20 cm (Figures 1D–1F), consistent with typical deep-sea sediment patterns.[23] Archaeal abundance declined more steeply than bacterial abundance (coefficients: −0.11 to −0.15 vs. −0.028 to −0.072). By contrast, the trench bottom station maintained stable microbial abundance (10^6–10^7 copies/g) throughout the sediment column (0–22 cm) (Figure 1G), suggesting that trench bottom environments buffer against typical depth-decay patterns[23] and preserve microbial biomass.

Metaproteomic measurement by nanoflow liquid chromatography-electrospray ionization tandem mass spectrometry (nLC-MS/MS) further revealed heterogeneity at the functional activity level (Figures 1D–1G). Across 50 sediment samples from the four representative stations, we detected 15,314 unique peptides with 263,698 total unique peptide-spectrum matches (PSMs) (STAR Methods). Consistent with qPCR data, the trench bottom station maintained high protein diversity (median 1,253 unique peptides per sample) throughout the sediment column (Figure 1G), whereas slope and abyssal sites showed steep functional decay from >1,000 unique peptides per sample at the surface (0–2 cm) to <100 unique peptides below 2 cm (Figures 1D–1F). Notably, between two neighboring stations from Dive FDZ072 with similar water depth, site FDZ072A in the fault valley retained 80–100 unique peptides per sample (Figure 1F), whereas only 10 detectable unique peptides retained at site FDZ072E on the adjacent fault scarp (Figures 1B and 1E), suggesting that substantial activity heterogeneity exists even among sites at comparable depths within a single dive. Together, these results demonstrate that both microbial biomass and functional activity vary substantially across hadal topographic settings, establishing the foundation for integrated geochemical and multi-omics analyses of topography-related microbial heterogeneity in subsequent sections.

Topography as an overlooked determinant of geochemical and microbial heterogeneity

To quantitatively characterize topographic settings, we calculated the topographic position index (TPI) from high-resolution seafloor bathymetry (STAR Methods), where negative TPI values indicate low-lying concave positions and positive values correspond to ridge-like convex positions (Figure 2A). To examine topography-microbiome relationships, we integrated geochemical profiles, metagenomes, metaproteomes across 11 sampling positions from the four topography-targeted dives (STAR Methods).

Geochemical profiling revealed substantial environmental heterogeneity at both large and fine scales (Figures 2B–2E and S1). Redundancy analysis (RDA) showed that water depth was negatively associated with porewater dissolved O_2 (DO), NO_2^-, NH_4^+, and solid-phase δ^{15}N-TN, primarily reflecting steep redox gradients from aerobic to anaerobic conditions at trench bottom locations, where O_2 and NO_3^- were depleted below 20 cm sediment depth (Figures 2B and S1A). Meanwhile, TPI and sediment depth were positively associated with porewater concentration of NO_3^- and SO_4^{2-}, but negatively associated with solid-phase total organic carbon (TOC), total nitrogen (TN), TOC/TN, and δ^{13}C-TOC, reflecting their roles in governing electron acceptor and nutrient availability (Figures 2B and S1A).

Notably, although stable isotope mixing models indicated consistently >90% marine origin for organic matter across all locations (Figures S1B and S1C) (STAR Methods), sites within the same dive (at similar water depths) exhibited contrasting organic content and quality (Figures 2C and 2D). Some locations retained higher TOC (>0.3%) and TOC/TN (>6.5) with δ^{13}C-TOC values typical of fresh marine organic matter (−19‰ to −23‰),[11] corresponding to negative TPI values indicative of concave locations. By contrast, neighboring locations showed lower TOC (0.1%–0.3%) and TOC/TN (2.5–6) with more depleted δ^{13}C-TOC (−26‰ to −23‰), indicative of refractory residues after extensive degradation, and these consistently corresponded to convex positions (positive TPI). Since all sites share a common marine organic matter source, these contrasts suggest that fine-scale topography modulates organic matter retention and preservation.

Compared with water depth and sediment depth—the spatial variables conventionally associated with hadal microbial variation—TPI showed overall comparable correlations with both geochemical variables and microbial community composition and function. RDA showed that TPI explained the largest fraction of geochemical variance (adjusted R^2 = 16%), exceeding water depth (9%) and sediment depth (3%) (Figure 2E). TPI was significantly correlated with the greatest number of geochemical parameters among the three spatial variables, including positive associations with NO_3^-, DO, and δ^{15}N-TN, and negative associations with TOC, TOC/TN, and δ^{13}C-TOC (Spearman correlation, false discover rate (FDR)-adjusted $p < 0.01$; Figure 2E), reflecting the combined effects of oxidized and nutrient-limited conditions on high-TPI ridge-like convex locations. These TPI-linked geochemical parameters in turn showed significant correlations with metagenomic and metaproteomic community structure (permANOVA, $p < 0.01$; Figures 2E–2G), suggesting that topography shapes microbial communities in part through its influence on local geochemical conditions.

Consistently, non-metric multidimensional scaling (NMDS) ordination of metagenomes from the topography-targeted stations showed that microbial community composition co-varied with water depth, sediment depth, and TPI along distinct directions (Figure 2F). When considering the functionally active community through metaproteomic data, TPI emerged as a prominent vector separating functionally distinct communities (Figure 2G). At the trench-wide scale, NMDS of metagenomes from all 55 locations confirmed that TPI, water depth, and sediment depth each contributed to community structuring (Figure 2H). Variance partitioning further demonstrated that TPI independently explained 5% of metagenome variation, comparable to water depth (4%) and sediment depth (6%), with an additional 6% shared between TPI and water depth (Figure 2I). These results establish TPI as an overlooked yet important

(H) NMDS ordination of metagenome-based prokaryotic community dissimilarity across all trench-wide samples (n = 773, from 55 locations). Arrows represent spatial factors only, as geochemical measurements were not available for all sites.
(I) Variance partitioning of the three spatial factors in explaining trench-wide metagenome-based community composition. The overlap between TPI and other factors is highlighted.
See also Figure S1 and Table S2 for detailed geochemical measurements, Figure S2 for alpha diversity, and Figure S3 for taxonomic composition.

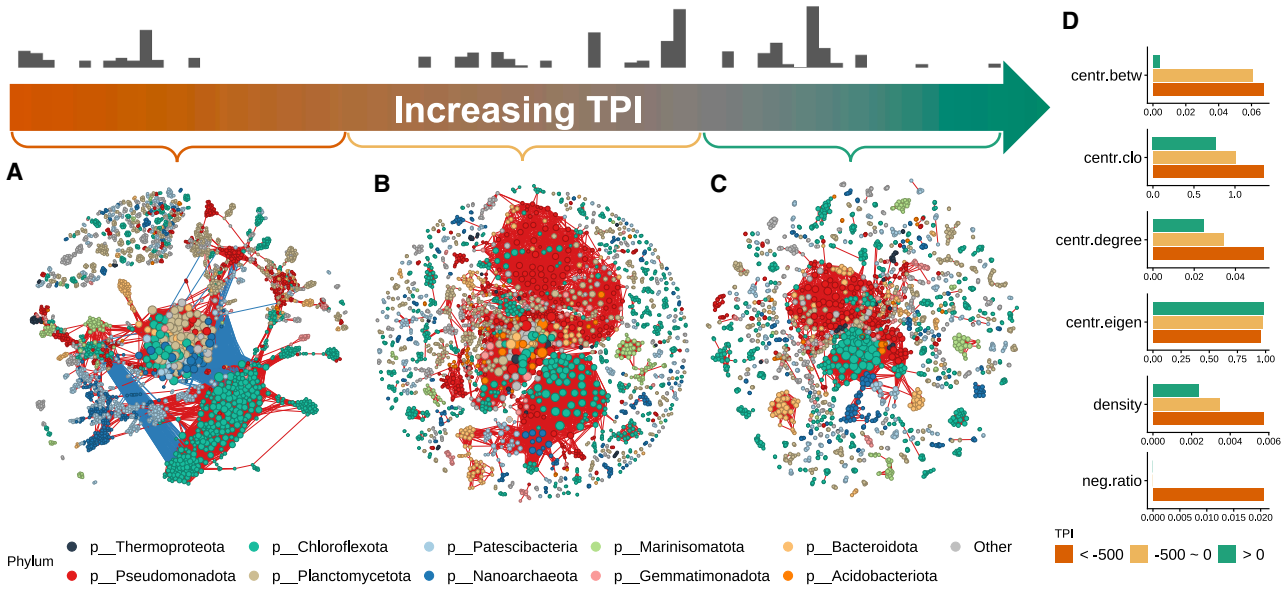

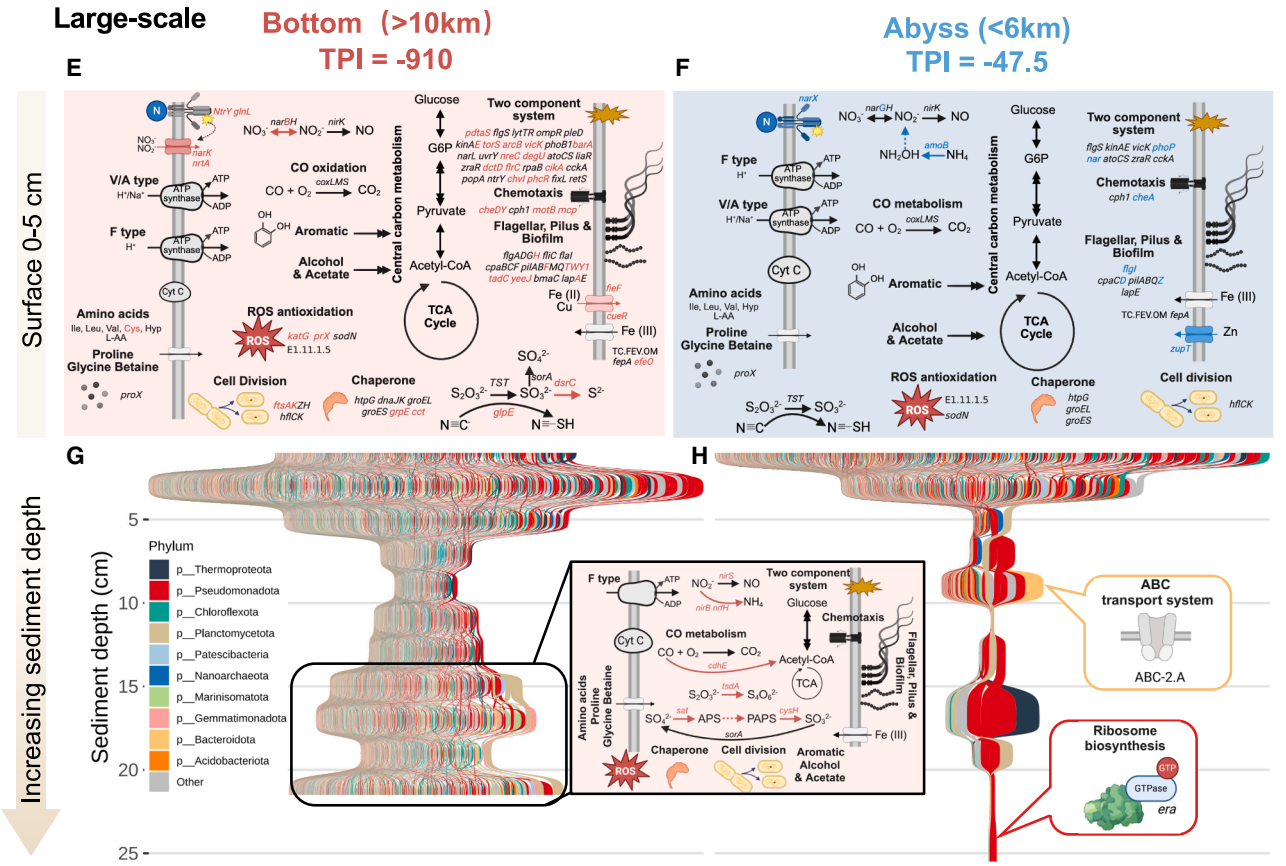

Figure 3. Topography-dependent microbial interaction networks and depth-stratified metabolic profiles

The arrow above (A)–(C) indicates increasing TPI from left to right, with the histogram illustrating the trench-wide TPI distribution of all samples, which naturally partitions into three groups.

(A–C) Co-occurrence networks of prevalent SRGs across the TPI gradient for all trench-wide samples: (A) TPI < −500, (B) −500 < TPI < 0, (C) TPI > 0. Nodes represent SRGs, colored by phylum affiliation. Red and blue edges indicate positive and negative correlations, respectively.

(D) Network-level centrality metrics for each network. Centr_betw: betweenness centrality; centr_clo: closeness centrality; centr_degree: degree centrality; centr_eigen: eigenvector centrality; density: network density; neg.ratio: proportion of negative correlations.

(E and F) Metaproteomic profiles of microbial metabolic capacities in surface sediments (0–5 cm) at the trench bottom (E) and abyssal site (F), showing shared foundational functions and location-specific enhanced capabilities (red and blue texts, respectively).

(legend continued on next page)

determinant of both geochemical environments and microbial community composition across hadal settings.

Topography structures microbial interaction complexity across the Mariana Trench

Beyond community composition, we examined whether topography influences microbial interaction patterns at the trench-wide scale. We constructed co-occurrence networks of prevalent species-level representative metagenome-assembled genomes (SRGs, present in at least 30% of samples) among the 86 sediment cores from 55 sampling sites along the TPI gradient, which naturally partitioned into three topographic groups: TPI < −500 (n = 215), TPI from −500 to 0 (n = 351), and TPI > 0 (n = 286) (STAR Methods; Figures 3A–3C). The networks revealed a topography-dependent gradient of microbial interaction complexity with increasing TPI, transitioning from densely connected and functionally differentiated communities to fragmented and cooperation-dominated communities, indicating that hadal topography shapes the ecological interaction architecture of sediment microbiomes beyond compositional differences.

The most negative TPI values correspond to the most deeply concave topographic positions, where the inferred microbial correlations were both the strongest and the most complex. The network for TPI < −500 displayed the highest network-level betweenness (0.07), closeness (1.35), and degree centrality (0.05), as well as the highest density (0.006) among the three groups (Figures 3A and 3D). This network also exclusively contained negative correlations (~2% of all connections), which, though rare, served as critical boundaries partitioning the network into two major modules, suggesting ecological differentiation between distinct microbial consortia at these deeply concave sites (Figure 3A). One module was primarily composed of Chloroflexota SRGs—a phylum widely distributed in marine environments and known to exhibit strong co-occurrence patterns that track local environmental conditions[20]—while the other comprised a mix of SRGs from Planctomycetota, Chloroflexota, Nanoarchaeota, Patescibacteria, Pseudomonadota, and Bacteroidota. Notably, a cluster of Nanoarchaeota and Patescibacteria SRGs co-varied with each other but remained distantly connected to other phyla, consistent with their specialized ecological niches enabled by streamlined genomes.[24,25]

The network for TPI from −500 to 0 displayed intermediate complexity, maintaining comparable betweenness centrality (0.06) to the previous network but lower closeness (1.00), degree centrality (0.03), and density (0.003) (Figures 3B and 3D). The core modules, especially the Chloroflexota-dominated module, were notably reduced in scale, with the proportion of highly connected nodes (degree > 10) in the network decreasing from 34% to 25%. The mixed-phyla module was also diminished, while Pseudomonadota SRGs substantially expanded around it, forming a prominent peripheral cluster (Figure 3B). The negative correlations that partitioned the previous network into distinct modules disappeared entirely, reflecting predominantly cooperative strategies in these hadal sedimentary environments.

Positive TPI values correspond to convex, ridge-like topographic positions, where inferred microbial interactions were the weakest and most fragmented. The network with TPI > 0 exhibited substantially reduced connectivity (Figure 3C). Only a subset of SRGs from Chloroflexota, Pseudomonadota, Bacteroidota, Acidobacteriota, and Thermoproteota formed a relatively cohesive network core, with Pseudomonadota SRGs largely replacing the mixed-phyla module observed in the concave networks, while the remaining SRGs were largely organized into numerous isolated taxon-specific clusters. This network displayed the lowest betweenness (0.004), closeness (0.77), and degree centrality (0.02), as well as the lowest density (0.002), indicating that most SRGs had few interaction partners and that the community lacked highly connected taxa capable of mediating broad ecological linkages (Figure 3D). The exclusively positive interactions within these fragmented communities suggest reliance on cooperative survival strategies to cope with limited nutrient supply and refractory organic matter typical of exposed convex positions, consistent with the geochemical patterns observed at these sites (Figures 2C and 2D). These interaction patterns, together with the geochemical and compositional evidence presented above, prompted us to further investigate how topographic settings shape active microbial metabolism through metaproteomic profiling.

The lowest TPI location at the trench bottom sustains the highest microbial activities

Among the 11 topography-targeted locations, the lowest TPI value (−910) occurred at the bottom of the Mariana Trench (FDZ070A, 10,888 m b.s.l.). In-depth metaproteomic analyses at this station revealed that, functionally, trench bottom microbiomes established specialized capabilities throughout the sediment column (Figures 3E and 3G). Surface layers (0–5 cm) harbored up to 1,500 SRGs with detected protein expression (hereafter termed functioning SRGs), exhibiting specialized capabilities in antioxidation systems (e.g., *katG* and *prX*), chaperone proteins (e.g., *dnaJK*, *grpE*, and *cct*), chemotaxis (e.g., *cheDY*, *motB*, and *mcp*), cell division (*ftsAKZH*), and biofilm formation (*tacC*, *yeeJ*, *bmaC*, and *lapA*), beyond the fundamental metabolic functions for microbial survival (Figure 3E). Most remarkably, diversified functioning communities persisted in deeper sediments (>15 cm), maintaining 745–1,059 functioning SRGs across 38–52 phyla (Figure 3G). Deep-layer communities sustained essential activities while developing anaerobic specializations, including nitrite reduction (*nirS*, *nirB*, and *nrfH*), carbon monoxide metabolism (*cdhE*), and sulfate reduction (*sat* and *cysH*), indicating successful adaptation to oxic-to-anoxic transitions with increasing sediment depth (Figure 3G). While elevated sedimentation rates at the trench bottom may contribute to this

(G and H) Sediment depth profiles of functioning SRGs along the sediment column at the trench bottom (G) and abyssal site (H). Each flow path represents one SRG, with width proportional to the total PSMs detected. The most active SRGs are positioned at the rightmost. Flow paths are colored by phylum, illustrating the maintenance of diverse active communities throughout the sediment column at the trench bottom compared with rapid functional attenuation at the abyssal site. Metabolic diagrams were created in BioRender. Zhao, W. (2026) https://BioRender.com/3gk8e1k.
See also Table S3.

pattern, the sustained expression of diverse metabolic genes across redox transitions suggests active microbial adaptation rather than passive biomass burial. This sustained metabolic diversity represents a fundamental departure from conventional deep-ocean sediment ecosystems,[26,27] confirming that trench bottom sediments sustain an active microbial ecosystem.[10,14]

By contrast, the abyssal stations at the rim of the Mariana Trench had moderate TPIs toward zero, consistent with the largely flat topography of the abyssal plain. The stark TPI contrast between the trench bottom and the abyssal plain mirrors the well-documented differences in microbial biomass and activity between these two depth zones,[10,14,16,18] providing an opportunity to examine how our metaproteomic data capture this established pattern. Metaproteomic analyses at the representative station (FDZ074A, 5,882 m b.s.l., TPI = −48) showed that microbial activity declined rapidly with sediment depth, with functioning SRGs dropping from 949 at the surface to fewer than 20 in deeper sediments (Figure 3H). Functionally, surface sediments (0–5 cm) maintained fundamental metabolic activities in metaproteomes, including aromatic compound utilization (*hcaC*), CO oxidation (*coxLMS*), nitrogen cycling (*narH* and *nirK*), and uptake of compatible solute glycine betaines (*proX*) (Figure 3F), essential for hadal survival.[20] However, deeper layers were restricted to basic cellular maintenance, including only ABC transport systems (*ABC-2.A*) in a Bacteroidota SRG and ribosome biosynthesis (*era*) in a Pseudomonadota SRG, alongside a few functionally uncharacterized proteins (Figure 3H). This rapid functional impoverishment illustrates the limited sustainability of microbial communities in abyssal environments, where flat topography provides neither the organic matter accumulation nor the physical protection afforded by concave hadal features.

Neighboring concave and convex locations harbor distinct microbial metabolic strategies on the slope

We next zoomed in on the comparison between two stations on the subduction slope from Dive FDZ072 that shared similar water depths but occupied opposing topographic extremes. Site FDZ072E (9,266 m b.s.l., TPI = 114) represented the highest TPI and thus the most convex position among all 11 topography-targeted stations, while site FDZ072A (9,556 m b.s.l., TPI = −383) was the most concave station within the same dive. Despite within less than 300 m difference in water depth, these two sites were separated by a TPI contrast of 497, offering an ideal comparison to illustrate fine-scale topographic effects on microbial metabolism.

At surface sediment layers (0–2 cm), both topographic settings shared some fundamental metabolic functions (Figure 4A), reflecting common adaptive responses to the extreme pressures and oligotrophic conditions imposed by similar water depths. These included carbon utilization (e.g., aromatic compounds), ATP synthase (both V/A type and F type), energy supply (e.g., CO oxidation and nitrate reduction), pressure adaptation (e.g., antioxidation, chaperone, and compatible solutes), and cell-cycle processes (e.g., DNA replication, transcription, and cell division). However, beyond these fundamental functions, each topographic feature exhibited distinct metabolic signatures and contrasting sediment depth-dependent activity patterns.

Concave sites: Extended microbial refugia beyond the trench bottom

Concave microbiomes established extended functional persistence with sustained metabolic capabilities throughout the sediment column. Surface layers (0–2 cm) showed enhanced regulatory and adaptive capabilities, including additional two-component systems for carbon storage (*barA*), biofilm formation and sporulation (*kinA* and *retS*), nitrogen metabolism regulation (*nreC* and *fixL*), and specialized DNA repair mechanisms (*radD* and *sbcD*) (Figure 4A). These functions indicate significant investment in environmental sensing, community development, and genetic integrity maintenance.

Most remarkably, concave sites maintained substantial metabolic activities throughout sediment depths. This sustained activity is consistent with the higher TOC content and fresher marine organic matter observed at concave sites (Figures 2C and 2D), which likely provide a more favorable substrate supply for microbial metabolism across sediment depths. At 2–4 cm sediment depth, 451 functioning SRGs preserved diverse metabolic capacities, including cell-cycle processes, stress adaptation, and comprehensive biogeochemical cycling (Figure 4B). Even at 18–20 cm sediment depth, concave sites demonstrated occasional metabolic activity blooms with 227 functioning SRGs expressing genes for regulatory systems, biofilm formation, nutrient uptake, and diverse carbon metabolism (Figure 4D). This sustained metabolic diversity represents extended microbial refugia on the slope beyond the trench bottom.

Convex sites: Stress-adapted but metabolically constrained

Convex microbiomes exhibited specialized adaptations to environmental stress but showed rapid functional decline with sediment depth. Surface layers (0–2 cm) showed enhanced sulfur metabolism (*sat*, *soxC*, and *TST*), alternative glycolysis (*aor*), heavy metal detoxification of mercury (*merA*) and arsenic (*arsC*), copper exfflux (*cueR*), reactive oxygen species (ROS) antioxidation (*sodN*, *SOD1*, *SOD2*, and enzyme E1.11.1.5), and enhanced motility through flagellar (*flgDK*, *fliCW*, and *flaI*) and pilus (*pilABMQV* and *cpaCDF*) proteins. These functional specificities reflect the adaptation to toxic stress conditions with enhanced detoxification and motility capabilities at the convex site (Figure 4A).

In contrast to the concave site, the convex microbiomes rapidly transitioned to metabolic constraint with increasing sediment depth. At 2–4 cm depth, only 92 functioning SRGs remained with severely limited metabolic capabilities, restricted to fundamental cellular maintenance processes, including basic regulatory systems, amino acid uptake, and ribosome biosynthesis (Figure 4C). In deeper sediment layers, functional gene expression was virtually eliminated, with only occasional detection of maintenance proteins (Figure 4E). This rapid functional collapse demonstrates that microbial communities at this convex site quickly shift to survival mode rather than sustaining active metabolism, reflecting the challenging environmental conditions typical of exposed ridge-like topographic positions.

Collectively, these findings reveal that slope concave sites function as previously unrecognized hotspots for microbial activities within hadal trenches, maintaining active biogeochemical cycling at depths where typical marine sediments become

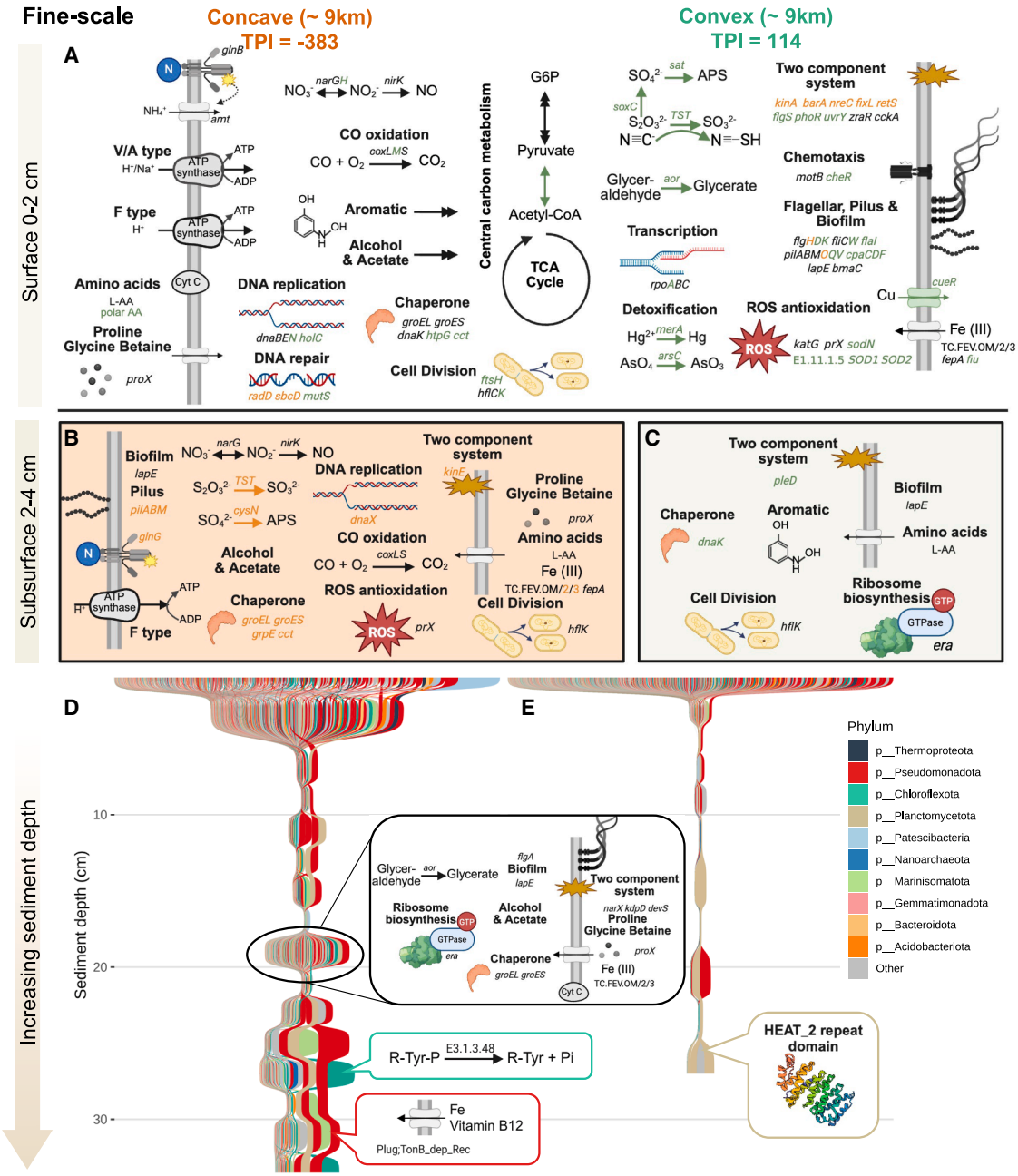

Figure 4. Fine-scale topography differentiates microbial metabolic strategies between neighboring sites on the trench slope

(A) Metaproteomic profiles of microbial metabolic capacities in surface sediments (0–2 cm) at concave site FDZ072A (TPI = −383) and convex site FDZ072E (TPI = 114). Site-specific genes were colored accordingly.

(B and C) Comparison of metabolic capacities in the 2–4 cm sediment layer at the concave (B) and convex (C) site.

(D and E) Sediment depth profiles of functioning SRGs along the sediment column at the concave (D) and convex (E) sites. Each flow path represents one SRG, with width proportional to the total PSMs detected. The most active SRGs are positioned at the rightmost. Flow paths are colored by phylum.

Metabolic diagrams were created in BioRender. Zhao, W. (2026) https://BioRender.com/3gk8e1k.

See also Table S3.

metabolically restricted. The contrast between metabolically constrained convex sites and thriving concave refugia demonstrates that fine-scale topography creates distinct microenvironmental niches that fundamentally reshape microbial ecosystem function in the deepest ocean.

Slope concave features mediate inferred microbial vertical dispersal

To elucidate the topographic effects driving spatial heterogeneity of microbiomes, we analyzed microbial dispersal patterns along the southern slope through mapping species

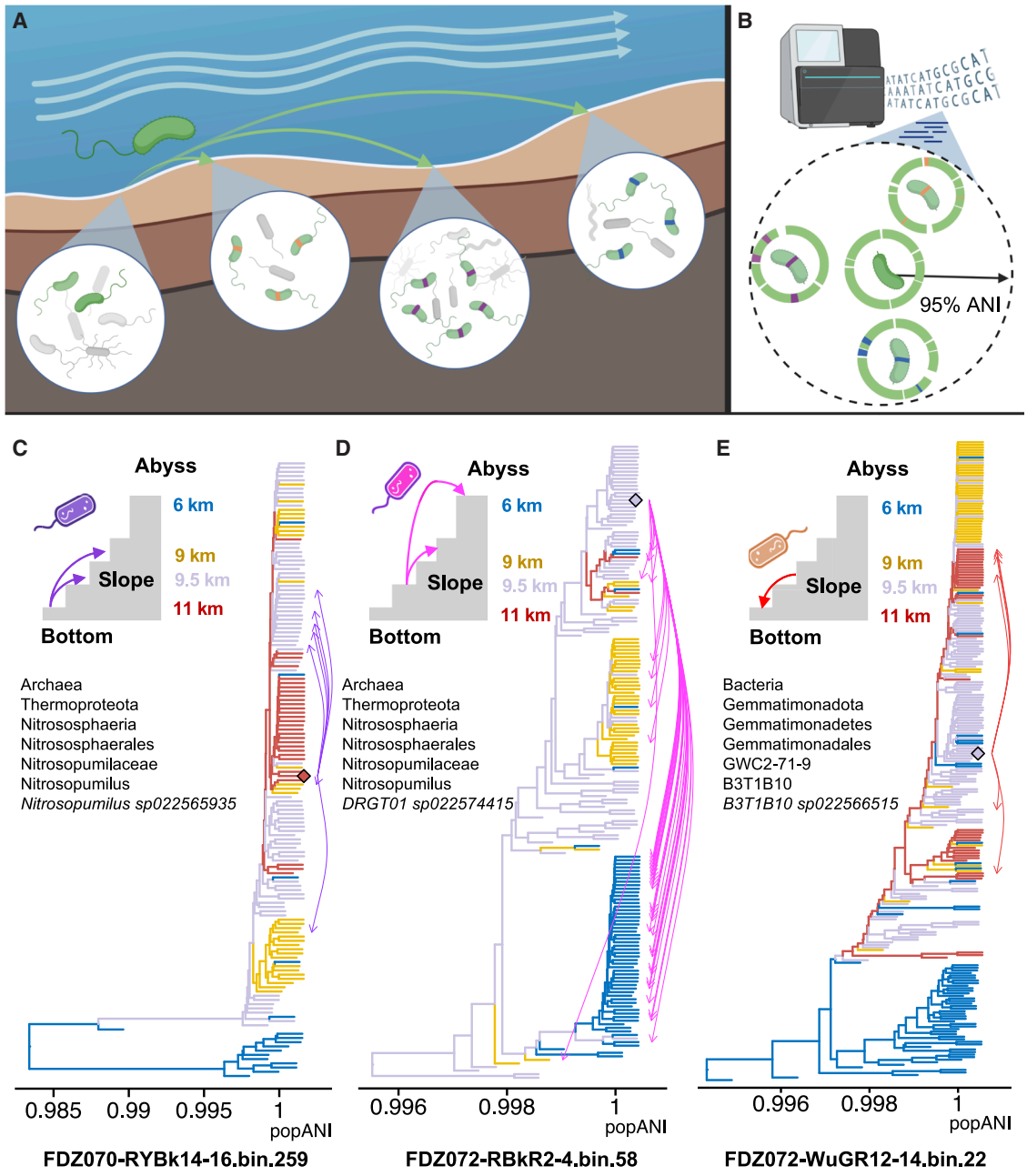

Figure 5. Concave locations mediate microbial vertical dispersal between the trench bottom and the abyssal regions

(A) Schematic representation of microbial dispersal potentially driven by hydrodynamic processes. Stochastic and selective mutations accumulate as microbial species disperse to different locations, generating intra-species microdiversity.

(B) Following metagenomic sequencing and downstream analyses, dispersed genomes carrying varying degrees of microdiversity are dereplicated into the same SRG within the 95% ANI species radius. The genome located at the center of the ANI cluster is selected as the representative, most likely reflecting the ancestral genome from which variants originated.

(C–E) Three distinct microbial dispersal patterns along the southern slope of the Mariana Trench, reconstructed based on genome microdiversity signatures. Arrows indicate the occurrence and direction of detected dispersal events. Dendrograms show pairwise population ANI (popANI) of the same SRG across all samples. Taxonomic nomenclature for each SRG is displayed from domain to species level.

(A) and (B) were created in BioRender. Zhao, W. (2026) https://BioRender.com/v58l247.

distributions and tracking evolutionary microdiversity within SRG lineages (STAR Methods). Unlike macrofauna, microorganisms have extremely limited motility, especially in sediments (1.2×10^{-5} cm^2 s^{-1}),[28] so their kilometer-scale distribution patterns primarily reflect passive dispersal through oceanographic processes.[29,30]

We developed an approach based on species-level intra-genomic microdiversity to reconstruct microbial dispersal

patterns. As a microbial species disperses from its source to various destinations, it accumulates mutations, generating a series of similar-but-not-identical genomes within the 95% average nucleotide identity (ANI) species delineation threshold[31] (Figure 5A). These genomes are dereplicated into the same SRG, whose representative most likely reflects the ancestral genome from which all variants originated (Figure 5B). Dispersal paths were then reconstructed from each SRG's source sample to all samples containing it, with directionality inferred using bootstrapped tests to mitigate stochastic noise (STAR Methods).

The majority of predicted dispersal events involved upward transport from deeper to shallower locations, with only limited downward dispersal inferred. Three distinct microbial dispersal patterns were revealed along the southern slope, characterized by their directional flow and source-sink relationships (Figure 5). The first pattern showed dispersal of an ammonia-oxidizing archaeal species, Nitrososphaeria FDZ070-RYBk14-16.bin.259, from the trench bottom (FDZ070A) to the slope faulting zones at 9–9.5 km b.s.l. (FDZ072C, FDZ069B, and FDZ069E) (Figure 5C). Genetic variations using population-level ANI (popANI)[32] showed that slope populations (FDZ072 and FDZ069) clustered together and maintained popANI > 0.995 with the trench bottom source (FDZ070), indicating well-preserved genetic similarity along the dispersal path. By contrast, abyssal populations (<6 km b.s.l., FDZ074) formed a separate clade with popANI < 0.985, showing greater genetic divergence outside the trench system.

A second upward pattern originated from slope concave locations: another Nitrososphaeria species (FDZ072-RBkR2-4.bin.58) dispersed from concave locations (FDZ072A) to flat (FDZ072C, FDZ069E) and convex locations (FDZ072E and FDZ069B) on the trench slope, extending to abyssal plains (FDZ074A and B) (Figure 5D). Notably, abyssal populations maintained popANI > 0.995 with the slope source and were nearly identical to each other, supporting their sole origin from the slope faulting zone. Both the first and second upward dispersal patterns together suggest that through slope-mediated vertical exchange, hadal microorganisms retain the potential to rejoin in upper oceanic ecosystems.

In contrast to the inferred upward dispersal patterns, downward dispersal was only observed from a slope flat location (FDZ072C) to a nearby concave location (FDZ072A) and finally arrived at trench bottoms (FDZ070A and E), involving a Gemmatimonadetes species (FDZ072-WuGR12-14.bin.22) (Figure 5E). This pattern likely represents microorganisms dispersed along lateral sediment transport toward the trench bottom, known as the "funneling effect." Again, we observed that the populations linked by the dispersal paths share popANI above 0.998, while those residing in other locations showed higher genetic divergence.

Collectively, these dispersal patterns indicate that fine-scale topographic features, particularly slope concave zones, function as microbial interchange hubs facilitating predominantly upward transport of hadal-adapted microorganisms, contributing to the vertical connectivity between hadal and broader oceanic zones.

Quantitative topographic modeling unveils the hidden microbial carbon turnover hotspots

To investigate how the observed variations in microbial ecosystems and their activities could impact hadal biogeochemical cycling, we applied a one-dimensional reactive-transport model[33] to estimate microbially mediated sedimentary biogeochemical reaction rates within each sediment core. The model was calibrated against measured geochemical profiles at 11 sites from the four topography-targeted dives (Figure 6A). The applied boundary conditions and model parameters (see STAR Methods for details) allowed simulations that matched the measured profiles of TOC, DO, NO_3^-, NO_2^-, NH_4^+, and SO_4^{2-} (Figure 6B for an example at site FDZ072A and Figure S4 for detailed comparisons). In particular, the simulated rates of nitrate reduction (using *narG* and *napA* as marker genes), denitrification (*norB*, *nosZ*, and *nirK*), dissimilatory nitrite reduction to ammonia (DNRA, *nrfA*, and *nirB*), ammonia oxidation (*amoA*), anammox (*hzsA*), sulfate reduction (*aprA* and *dsrB*), and sulfide oxidation (*sqr* and *soxB*) were calibrated to match the abundance variations of their corresponding marker genes in metagenomes across all 11 sites. Although metagenomic gene abundance does not directly represent metabolic activity, the expression of these marker genes was independently confirmed in metaproteomes at the four representative stations (Table S3), and the calibrated models successfully reproduced measured geochemical profiles across all sites (Figures 6B and S4), supporting the reliability of this approach. To avoid convergence to random local optima, model calibrations were powered by differential evolution optimization methods[34] and were performed ten times from random starting points for each site. Together, this integrated modeling framework provided robust estimates of *in situ* microbially mediated carbon, nitrogen, and sulfur cycling rates across diverse hadal topographic settings.

Topographic features control organic carbon influxes

Model calibration results revealed that organic carbon influxes into sediments were primarily correlated with the topographic index TPI values (linear regression $R^2 = 0.64$, $p < 0.01$; Figure 6C) over water depth (linear regression $R^2 = 0.09$, $p < 0.01$), modifying the previous assumption that hadal organic matter input focuses solely on increasing water depth.[35] A linear model was then established as shown in Equation 1. The corresponding intercept (d) in Equation 1 suggests that the baseline organic carbon influx into sediment is around 1.8×10^4 μmol $C \cdot m^{-2} \cdot yr^{-1}$, and the coefficient ($k$) indicates that a decrease of one unit in TPI (becoming more concave) would result in an additional influx of 27.4 μmol $C \cdot m^{-2} \cdot yr^{-1}$.

$$F_{OC} = k \cdot TPI + d, \quad \text{(Equation 1)}$$

wherein k is the slope term, representing the effective coefficient for TPI on organic carbon influx, and d is the intercept term, representing the organic carbon deposition background subject to the Challenger Deep, Mariana Trench.

According to Equation 1 and leveraging high-resolution bathymetry data with calculated TPI values (Figures 6E and 6F), we predicted the fine-scale spatial distribution of organic carbon influx across the Challenger Deep of the Mariana Trench (Figure 6G). We validated our modeling approach using a previously studied site (site BC11)[35] in the Mariana Trench to assess the reliability of our predictive results, finding that our predicted organic carbon influx (1.5×10^4 μmol $C \cdot m^{-2} \cdot yr^{-1}$) was very close to the reported value (1.3×10^4 μmol $C \cdot m^{-2} \cdot yr^{-1}$) in literature,[35] supporting the accuracy of our extrapolation.

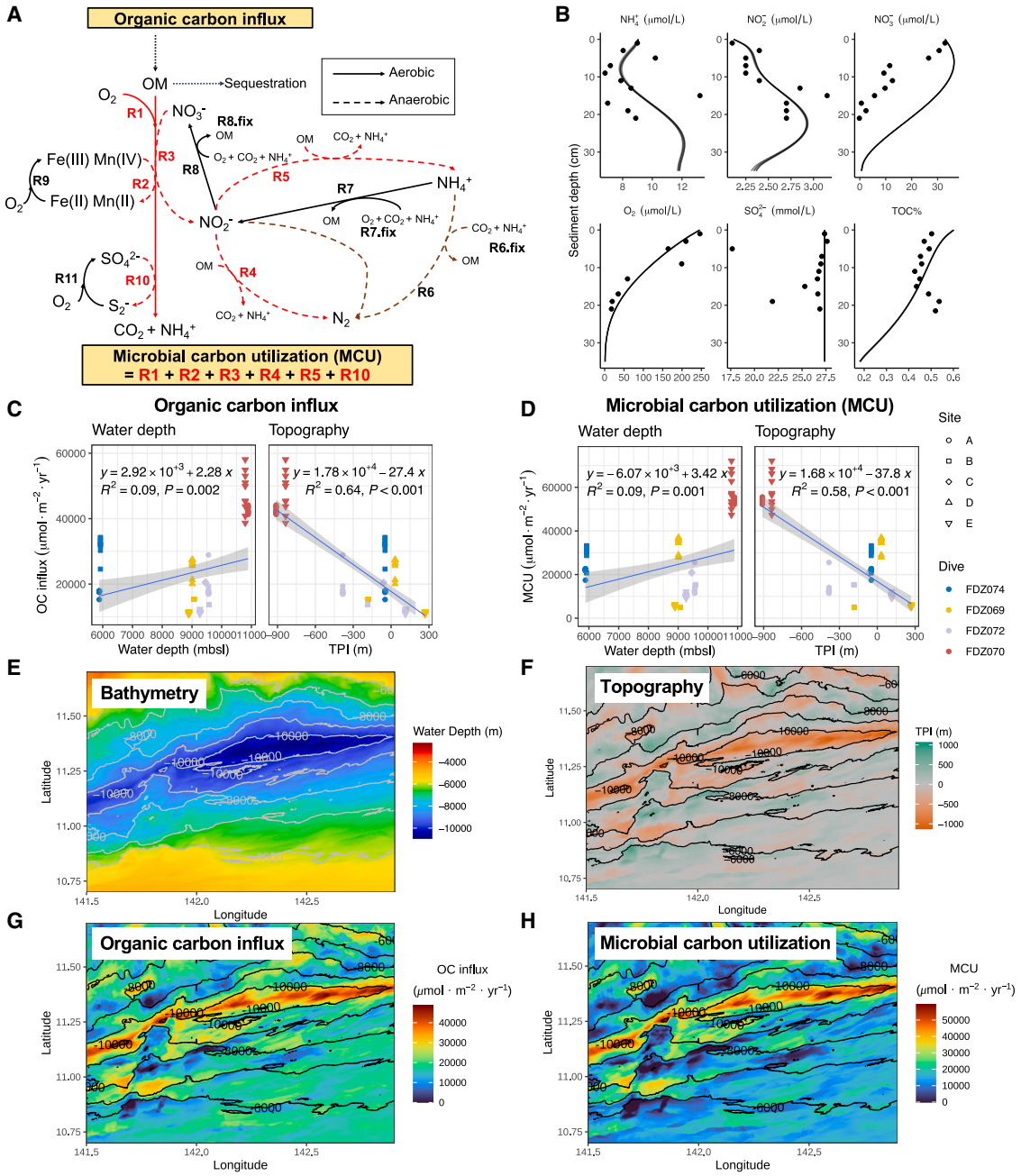

Figure 6. Quantitative assessment of topographic effects on organic carbon distribution and microbial biogeochemical processes reveals hidden microbial carbon turnover hotspots in the Mariana Trench

(A) Schematic diagram illustrating microbially mediated biogeochemical processes in sediments. We define the combination of six organic carbon utilization processes as the microbial carbon utilization (MCU) index to quantify the strength of microbial biogeochemical activities.

(B) Example of reactive-transport model predictions (curves) compared against measured geochemical profiles (dots) at site FDZ070A. Model calibration was performed ten times.

(C and D) Modeled (C) organic carbon influx into sediments and (D) MCU integrated within the 0–35 cm sediment depth interval at 11 locations as a function of corresponding water depth and topography. Results from 10 repeated model calibrations are shown. R-squared value represents the fraction of variance explained by the linear model, while the p-value measures its statistical significance.

(E and F) High-resolution bathymetry data and (F) topographic TPI values calculated from these bathymetric measurements.

(G) Spatial extrapolation of organic carbon influx based on its linear relationship with TPI shown in (C) and the TPI distribution in (F).

(H) Spatial extrapolation of MCU based on its linear relationship with TPI shown in (D) and the TPI distribution in (F).

See also Figures S4 and S5.

Given that an average of 4.6 $\times 10^4$ μmol C · m^{-2} · yr^{-1} of particulate organic carbon sinks into the Mariana Trench from surface water,[8] our estimations reveal that under baseline conditions, 39.1% of this particulate organic carbon accumulates in hadal sediments. However, fault zone topography on the slope generates several hotspots where organic carbon influx exceeds 3 $\times$ 10^4 μmol C · m^{-2} · yr^{-1}, corresponding to 65.2% of sinking organic carbon (Figure 6G). These results demonstrate that fine-scale topographic features actively redistribute carbon inputs, subsequently shaping the activities and succession patterns of hadal benthic microbiomes.

Concave topography incubates MCU hotspots

Topographic quantification further enabled assessment of microbial metabolic activities and microbially driven hadal biogeochemical processes. After model calibration for each sediment core, we defined the integrated flux of TOC utilization processes—including aerobic respiration, Mn/Fe reduction, nitrate reduction, denitrification, DNRA, and sulfate reduction—within the 0–35 cm sediment depth interval as the microbial carbon utilization (MCU) rate to quantify microbially mediated processes in hadal sediments.

We also observed that TPI, over water depth, was primarily related to the MCU rate (linear regression R^2 = 0.58 vs. 0.09, $p < 0.01$ for both cases; Figures 6D and S5). This correlation indicated that microbial activities were intensified in concave locations with negative TPI values but were restricted in convex locations with positive TPI values. This linear model (Equation 2) explained 58% of the variance in MCU. The coefficient (*a*) suggests that a decrease of one unit in TPI (becoming more concave) would result in an enhancement of 37.8 μmol C · m^{-2} · yr^{-1} in MCU. The intercept term (*b*) was 1.7 $\times$ 10^4 μmol C · m^{-2} · yr^{-1}, representing the background sedimentary microbial activity within the surface 35 cm in the Mariana Trench.

$$MCU = a \cdot TPI + b, \quad \text{(Equation 2)}$$

wherein *a* is the slope term, representing the effective coefficient for TPI on MCU, and *b* is the intercept term, representing the microbial metabolic background subject to the Mariana Trench.

Using Equation 2, we extrapolated the estimation of MCU across the Challenger Deep of the Mariana Trench based on measured TPI (Figure 6H). Our extrapolated MCU values showed good agreement with *in situ* measurements. For example, our estimations of MCU were 5.0 $\times$ 10^4 μmol C · m^{-2} · yr^{-1}at a bottom site and 2.3 $\times 10^4$ μmol C · m^{-2} · yr^{-1} at an abyssal site, which are quite comparable to the previous measurements at the same sites by using *in situ* O_2 consumption as a proxy for microbial activity.[14]

Remarkably, our topography-based modeling approach uncovered numerous previously unrecognized microbial activity hotspots scattered throughout the trench system. The largest MCU value in concave locations on the slope was 5.9 $\times$ 10^4 μmol C · m^{-2} · yr^{-1}, much higher than the average value of 1.8 $\times 10^4$ μmol C · m^{-2} · yr^{-1} in the studied trench area. These inferences demonstrate that fine-scale topographic features incubated previously invisible hotspots for microbially mediated biogeochemical processes distributed along the trench slope beyond trench bottoms (Figure 6H), which had been systematically overlooked before.

DISCUSSION

In this study, we conducted topographic-targeted HOV dives and centimeter-level sampling to examine topographic effects on microbial ecosystems and their activities at 6–11 km water depth along the subduction zone in the Mariana Trench. By integrating comprehensive multi-omics (metagenomics and metaproteomics) approaches and biomass quantifications with detailed geophysical mapping and geochemical analyses, we demonstrated that hadal trench microbial ecosystems are shaped by complex fine-scale topographical structures, extending beyond the traditional conceptualization of hadal trenches as simple "smooth V-shaped funnels."[1,11,36] These fine-scale topographic variations create distinct microenvironments with significantly different organic carbon influxes, substrate bioavailability, and redox conditions. Such topographically associated environmental heterogeneity promotes remarkable microbial variability in both composition and activity even among neighboring locations at similar water depths, indicating that water depth alone is insufficient to account for microbial distribution and activity in hadal environments.[17,35,37] These findings extend microbial biogeography principles beyond water depth to Earth's deepest accessible ecosystems.

Departing from the conventional sediment-depth-dependent decay pattern in marine sediments,[23,25] our results demonstrate sustained microbial biomass, diversity, and functional activity at concave locations throughout the sediment column. We attribute this primarily to the depositional nature of concave topography, which preferentially traps settling particles, retains labile organic matter, and provides physical shielding from currents and slope instabilities.[8] The resulting elevated substrate availability drives rapid electron acceptor consumption, establishing steep redox gradients that support stratified metabolic niches from aerobic at the surface to anaerobic processes at depth. Convex locations, by contrast, are prone to sediment erosion and limited organic matter retention due to their exposed geometry,[8,21] imposing nutrient scarcity that selects for stress-tolerant but metabolically constrained communities. A natural question is whether these contrasts simply reflect differences in sediment accumulation history between topographic positions.[38–40] For instance, convex sites with slow deposition may expose sediments with long burial histories where microbial activity has naturally declined, while concave sites with rapid accumulation may simply contain younger sediments where microbes have not yet exhausted available substrates. However, our metaproteomic data indicate that sedimentation history is not the sole explanation: distinct metabolic signatures were already evident at the sediment surface (0–2 cm) between neighboring stations FDZ072A and FDZ072E, where burial age should be negligible at both sites. This indicates that contemporary topography-associated geochemical differentiation already influences active microbial metabolism beyond the contribution of differential sedimentation rates.

In addition to the influence on local microbial communities, our dispersal inference revealed that the Mariana Trench is not as isolated as conventionally assumed but actively exchanges microorganisms with shallower oceanic environments. While previous research has shown that fine-scale topography modulates

the downward transport of organic matter along trench slopes—with concave features trapping and convex features deflecting settling particles[21]—our results reveal that topography may also shape an unexpected upward-dominant microbial dispersal toward the southern rim. This upward transport likely results from the combined effects of bioturbation,[41] current fluctuation,[8] sediment resuspension,[42] and seismic activities[43] in the hadal environment, supported by geophysical observations of tidal-induced turbulent mixing along the Mariana Trench flanks.[44] Microorganisms engaged in this inferred dispersal pattern exhibit genetic similarities between hadal and non-hadal subpopulations, suggesting potential interchange between these depth zones. These observations suggest that hadal trenches may participate in deep-ocean microbial biogeography more actively than previously assumed.

Topographic indices such as TPI could serve as integrative proxies that encapsulate multiple underlying processes—including geological activity, fluid dynamics, current variations, and sedimentation rates.[1,8,9] Our analyses further reveal extensive correlations between TPI and geochemical parameters, microbial biomass, community activities, and biogeochemical rates. While these individual environmental and microbial factors are difficult to measure comprehensively in hadal environments, TPI provides readily accessible surrogates for characterizing microbial functional activity and biogeochemical outcomes, particularly where large-scale acquisition of multi-omics and geochemical measurements remains prohibitively challenging.[3,11,22] Building on this rationale, we established the modeling framework linking MCU to topography (Equation 2, $MCU = a \cdot TPI + b$). Whether this relationship reflects a general property of seafloor ecosystems or is specific to the Mariana Trench remains an open question. Future systematic comparisons across different trench systems and broader seafloor environments will be essential to test the generalizability of this framework, ultimately contributing to a more comprehensive understanding of benthic microbial contributions to global elemental cycling.

RESOURCE AVAILABILITY

Lead contact

Requests for further information and resources should be directed to and will be fulfilled by the lead contact, Xiang Xiao (zjxiao2018@sjtu.edu.cn).

Materials availability

This study did not generate any new, unique reagents.

Data and code availability

- Metagenomic data can be viewed in NODE (http://www.biosino.org/node) by pasting the accession OEP004067 into the text search box or through the URL: https://www.biosino.org/node/project/detail/OEP004067.
- The mass spectrometry proteomics data have been deposited in the ProteomeXchange Consortium (http://proteomecentral.proteomexchange.org) via the iProX partner repository (https://www.iprox.cn/) with the dataset identifier PXD065548.
- Data and code to reproduce the results in this work were deposited in the SCIDATA of Shanghai Jiao Tong University (https://scidata.sjtu.edu.cn/records/tqazd-was05) and are also available through the Common Science and Technology Resource (CSTR) identification (https://cstr.cn/32010.11.sjtu.scidata.00000061).
- R package ProPopMove was hosted on GitHub (https://github.com/zhenjiaofenjie/ProPopMove). The exact version used in this study was deposited in Zenodo (https://doi.org/10.5281/zenodo.15877169).
- Any additional information required to reanalyze the data reported in this paper is available from the lead contact upon request.

ACKNOWLEDGMENTS

We extend our profound appreciation to the Institute of Deep-sea Science and Engineering, Chinese Academy of Sciences (IDSSE CAS), for providing critical access to R/V Tan Suo Yi Hao, as well as the HOV Fen Dou Zhe. The operational expertise and technical support from the crews and engineers were indispensable to the data acquisition and experimental success of this study. This work was financially supported by the National Key R&D Program of China (grant no. 2022YFC2805404), the National Natural Science Foundation of China (grant nos. 42330206, 32530002, 32570058, 92451301), the Project of State Key Laboratory of Microbial Metabolism, Shanghai Jiao Tong University (No. SKLMMZD_02), and the Startup Fund for Young Faculty at SJTU (SFYF at SJTU). Author Xiang Xiao is a SANS Exploration Scholar. We also thank Dr. Taoran Song from Hainan Tropical Ocean University for her help in map visualization for this manuscript. We also thank Dr. Jingli Hou, associate researcher from the Instrumental Analysis Center of Shanghai Jiao Tong University for her contributions to optimizing enzymatic cleavage methods for proteins and conducting mass spectrometry analysis of peptides. We acknowledge support from the Center for High Performance Computing (HPC) at Shanghai Jiao Tong University. We acknowledge support from the Ministry of Education of China, through the Extremophile Resource Division of the Engineered Microorganisms and Genetic Tools Collection Center of China (EMTCC), hosted at Shanghai Jiao Tong University.

AUTHOR CONTRIBUTIONS

Conceptualization, X.X., W.Z., C.C., and J.W.; methodology, J.W., C.C., and W.Z.; software, J.W., Q.Q., and A.H.; investigation, W.Z., C.C., X.X., A.J., Y.W., Y.C., W.S., and L.D.; resources, X.X., C.C., and W.Z.; formal analysis, W.Z., J.W., Q.Q., and A.H.; visualization, W.Z., J.W., and C.C.; data curation, W.Z., J.W., and A.H.; writing – original draft, W.Z. and J.W.; writing – review & editing, W.Z., J.W., X.X., C.C., and Y.Z.; funding acquisition, X.X. and W.Z.; supervision, X.X. and W.Z.

DECLARATION OF INTERESTS

The authors declare no competing interests.

DECLARATION OF GENERATIVE AI AND AI-ASSISTED TECHNOLOGIES IN THE WRITING PROCESS

During the preparation of this work, the authors used Claude (Anthropic) in order to assist with language polishing and manuscript editing. After using this tool, the authors reviewed and edited the content as needed and take full responsibility for the content of the publication.

STAR★METHODS

Detailed methods are provided in the online version of this paper and include the following:

- KEY RESOURCES TABLE
- EXPERIMENTAL MODEL AND STUDY PARTICIPANT DETAILS
- METHOD DETAILS
  - Geochemical measurements and analyses
  - Topographic data analysis and modeling
  - Metagenomic analyses
  - Community diversity analyses
  - Protein extraction
  - Enzymatic cleavage of proteins and purification of peptides
  - Mass spectrometry data acquisition

- Metaproteomic searching, peptide validation, protein inference and quantification
- Estimations of microbial population dispersal
- Biogeochemical modeling

- QUANTIFICATION AND STATISTICAL ANALYSIS

SUPPLEMENTAL INFORMATION

Supplemental information can be found online at https://doi.org/10.1016/j.chom.2026.06.015.

Received: April 22, 2026
Revised: May 24, 2026
Accepted: June 23, 2026
Published: July 20, 2026

REFERENCES

1. Jamieson, A.J., Fujii, T., Mayor, D.J., Solan, M., and Priede, I.G. (2010). Hadal trenches: the ecology of the deepest places on Earth. Trends Ecol. Evol. *25*, 190–197. https://doi.org/10.1016/j.tree.2009.09.009.
2. Stern, R.J. (2021). Ocean Trenches. In Encyclopedia of Geology, Second Edition, D. Alderton and S.A. Elias, eds. (Academic Press), pp. 845–854. https://doi.org/10.1016/B978-0-08-102908-4.00099-0.
3. Du, M., Peng, X., Zhang, H., Ye, C., Dasgupta, S., Li, J., Li, J., Liu, S., Xu, H., Chen, C., et al. (2021). Geology, environment, and life in the deepest part of the world's oceans. Innovation (Camb) *2*, 100109. https://doi.org/10.1016/j.xinn.2021.100109.
4. Masson, D.G. (1991). Fault patterns at outer trench walls. Mar. Geophys. Res. *13*, 209–225. https://doi.org/10.1007/BF00369150.
5. Oakley, A.J., Taylor, B., and Moore, G.F. (2008). Pacific Plate subduction beneath the central Mariana and Izu-Bonin fore arcs: New insights from an old margin. Geochem. Geophys. Geosyst. *9*, n/a–n/a. https://doi.org/10.1029/2007GC001820.
6. Boston, B., Moore, G.F., Nakamura, Y., and Kodaira, S. (2014). Outer-rise normal fault development and influence on near-trench décollement propagation along the Japan Trench, off Tohoku. Earth Planets Space *66*, 135. https://doi.org/10.1186/1880-5981-66-135.
7. Emry, E.L., Wiens, D.A., and Garcia-Castellanos, D. (2014). Faulting within the Pacific plate at the Mariana Trench: Implications for plate interface coupling and subduction of hydrous minerals. JGR Solid Earth *119*, 3076–3095. https://doi.org/10.1002/2013JB010718.
8. Stewart, H.A., and Jamieson, A.J. (2018). Habitat heterogeneity of hadal trenches: Considerations and implications for future studies. Prog. Oceanogr. *161*, 47–65. https://doi.org/10.1016/j.pocean.2018.01.007.
9. Oguri, K., Masqué, P., Zabel, M., Stewart, H.A., MacKinnon, G., Rowden, A.A., Berg, P., Wenzhöfer, F., and Glud, R.N. (2022). Sediment Accumulation and Carbon Burial in Four Hadal Trench Systems. J. Geophys. Res.: Biogeosci. *127*, e2022. https://doi.org/10.1029/2022JG006814.
10. Glud, R.N., Berg, P., Thamdrup, B., Larsen, M., Stewart, H.A., Jamieson, A.J., Glud, A., Oguri, K., Sanei, H., Rowden, A.A., et al. (2021). Hadal trenches are dynamic hotspots for early diagenesis in the deep sea. Commun. Earth Environ. *2*, 1–8. https://doi.org/10.1038/s43247-020-00087-2.
11. Xu, Y., Ge, H., and Fang, J. (2018). Biogeochemistry of hadal trenches: Recent developments and future perspectives. Deep Sea Res. II *155*, 19–26. https://doi.org/10.1016/j.dsr2.2018.10.006.
12. Kawagucci, S., Yoshida, Y.T., Noguchi, T., Honda, M.C., Uchida, H., Ishibashi, H., Nakagawa, F., Tsunogai, U., Okamura, K., Takaki, Y., et al. (2012). Disturbance of deep-sea environments induced by the M9.0 Tohoku Earthquake. Sci. Rep. *2*, 270. https://doi.org/10.1038/srep00270.
13. Bao, R., Strasser, M., McNichol, A.P., Haghipour, N., McIntyre, C., Wefer, G., and Eglinton, T.I. (2018). Tectonically-triggered sediment and carbon export to the Hadal zone. Nat. Commun. *9*, 121. https://doi.org/10.1038/s41467-017-02504-1.
14. Glud, R.N., Wenzhöfer, F., Middelboe, M., Oguri, K., Turnewitsch, R., Canfield, D.E., and Kitazato, H. (2013). High rates of microbial carbon turnover in sediments in the deepest oceanic trench on Earth. Nat. Geosci. *6*, 284–288. https://doi.org/10.1038/ngeo1773.
15. Wenzhöfer, F., Oguri, K., Middelboe, M., Turnewitsch, R., Toyofuku, T., Kitazato, H., and Glud, R.N. (2016). Benthic carbon mineralization in hadal trenches: Assessment by in situ O2 microprofile measurements. Deep Sea Res. I *116*, 276–286. https://doi.org/10.1016/j.dsr.2016.08.013.
16. Cui, G., Li, J., Gao, Z., and Wang, Y. (2019). Spatial variations of microbial communities in abyssal and hadal sediments across the Challenger Deep. PeerJ *7*, e6961. https://doi.org/10.7717/peerj.6961.
17. Zhou, Y.-L., Mara, P., Cui, G.-J., Edgcomb, V.P., and Wang, Y. (2022). Microbiomes in the Challenger Deep slope and bottom-axis sediments. Nat. Commun. *13*, 1515. https://doi.org/10.1038/s41467-022-29144-4.
18. Hiraoka, S., Hirai, M., Matsui, Y., Makabe, A., Minegishi, H., Tsuda, M., Juliarni, R., Rastelli, E., Danovaro, R., Corinaldesi, C., et al. (2020). Microbial community and geochemical analyses of trans-trench sediments for understanding the roles of hadal environments. ISME J. *14*, 740–756. https://doi.org/10.1038/s41396-019-0564-z.
19. Liu, S., and Peng, X. (2019). Organic matter diagenesis in hadal setting: Insights from the pore-water geochemistry of the Mariana Trench sediments. Deep Sea Res. I *147*, 22–31. https://doi.org/10.1016/j.dsr.2019.03.011.
20. Xiao, X., Zhao, W., Song, Z., Qi, Q., Wang, B., Zhu, J., Lin, J., Wang, J., Hu, A., Huang, S., et al. (2025). Microbial ecosystems and ecological driving forces in the deepest ocean sediments. Cell *188*, 1363–1377.e9. https://doi.org/10.1016/j.cell.2024.12.036.
21. Ichino, M.C., Clark, M.R., Drazen, J.C., Jamieson, A., Jones, D.O.B., Martin, A.P., Rowden, A.A., Shank, T.M., Yancey, P.H., and Ruhl, H.A. (2015). The distribution of benthic biomass in hadal trenches: A modelling approach to investigate the effect of vertical and lateral organic matter transport to the seafloor. Deep Sea Res. I *100*, 21–33. https://doi.org/10.1016/j.dsr.2015.01.010.
22. Feng, J.-C., Liang, J., Cai, Y., Zhang, S., Xue, J., and Yang, Z. (2022). Deep-sea organisms research oriented by deep-sea technologies development. Sci. Bull. *67*, 1802–1816. https://doi.org/10.1016/j.scib.2022.07.016.
23. Hoshino, T., and Inagaki, F. (2019). Abundance and distribution of Archaea in the subseafloor sedimentary biosphere. ISME J. *13*, 227–231. https://doi.org/10.1038/s41396-018-0253-3.
24. Tian, R., Ning, D., He, Z., Zhang, P., Spencer, S.J., Gao, S., Shi, W., Wu, L., Zhang, Y., Yang, Y., et al. (2020). Small and mighty: adaptation of superphylum Patescibacteria to groundwater environment drives their genome simplicity. Microbiome *8*, 51. https://doi.org/10.1186/s40168-020-00825-w.
25. Hoshino, T., Doi, H., Uramoto, G.-I., Wörmer, L., Adhikari, R.R., Xiao, N., Morono, Y., D'Hondt, S., Hinrichs, K.-U., and Inagaki, F. (2020). Global diversity of microbial communities in marine sediment. Proc. Natl. Acad. Sci. USA *117*, 27587–27597. https://doi.org/10.1073/pnas.1919139117.
26. Hoehler, T.M., and Jørgensen, B.B. (2013). Microbial life under extreme energy limitation. Nat. Rev. Microbiol. *11*, 83–94. https://doi.org/10.1038/nrmicro2939.
27. Bradley, J.A., Arndt, S., Amend, J.P., Burwicz, E., Dale, A.W., Egger, M., and LaRowe, D.E. (2020). Widespread energy limitation to life in global subseafloor sediments. Sci. Adv. *6*, eaba0697. https://doi.org/10.1126/sciadv.aba0697.
28. Fenchel, T. (2008). Motility of bacteria in sediments. Aquat. Microb. Ecol. *51*, 23–30. https://doi.org/10.3354/ame01182.
29. Mullane, K.K., Nishiyama, M., Kurihara, T., and Bartlett, D.H. (2023). Compounding deep sea physical impacts on marine microbial motility. Front. Mar. Sci. *10*. https://doi.org/10.3389/fmars.2023.1181062.

30. Grossart, H., Riemann, L., and Azam, F. (2001). Bacterial motility in the sea and its ecological implications. Aquat. Microb. Ecol. *25*, 247–258. https://doi.org/10.3354/ame025247.

31. Olm, M.R., Brown, C.T., Brooks, B., and Banfield, J.F. (2017). dRep: a tool for fast and accurate genomic comparisons that enables improved genome recovery from metagenomes through de-replication. ISME J. *11*, 2864–2868. https://doi.org/10.1038/ismej.2017.126.

32. Olm, M.R., Crits-Christoph, A., Bouma-Gregson, K., Firek, B.A., Morowitz, M.J., and Banfield, J.F. (2021). inStrain profiles population microdiversity from metagenomic data and sensitively detects shared microbial strains. Nat. Biotechnol. *39*, 727–736. https://doi.org/10.1038/s41587-020-00797-0.

33. Soetaert, K., and Meysman, F. (2009). ReacTran: Reactive Transport Modelling in 1d, 2d and 3d. https://doi.org/10.32614/CRAN.package.ReacTran.

34. Ardia, D., Boudt, K., Carl, P., Mullen, K., and Peterson, B. (2011). Differential Evolution with DEoptim. R J. *3*, 27. https://doi.org/10.32614/RJ-2011-005.

35. Luo, M., Gieskes, J., Chen, L., Shi, X., and Chen, D. (2017). Provenances, distribution, and accumulation of organic matter in the southern Mariana Trench rim and slope: Implication for carbon cycle and burial in hadal trenches. Mar. Geol. *386*, 98–106. https://doi.org/10.1016/j.margeo.2017.02.012.

36. Glud, R.N., and Schauberger, C. (2024). Element cycling and microbial life in the hadal realm. Trends Microbiol. *32*, 1045–1048. https://doi.org/10.1016/j.tim.2024.07.004.

37. Peoples, L.M., Donaldson, S., Osuntokun, O., Xia, Q., Nelson, A., Blanton, J., Allen, E.E., Church, M.J., and Bartlett, D.H. (2018). Vertically distinct microbial communities in the Mariana and Kermadec trenches. PLOS One *13*, e0195102. https://doi.org/10.1371/journal.pone.0195102.

38. Liu, J., Li, D.-W., He, X., Liu, R., Cheng, H., Su, C., Chen, M., Wang, Y., Zhao, Z., Xu, H., et al. (2024). A unique subseafloor microbiosphere in the Mariana Trench driven by episodic sedimentation. Mar. Life Sci. Technol. *6*, 168–181. https://doi.org/10.1007/s42995-023-00212-y.

39. Orsi, W.D. (2018). Ecology and evolution of seafloor and subseafloor microbial communities. Nat. Rev. Microbiol. *16*, 671–683. https://doi.org/10.1038/s41579-018-0046-8.

40. Starnawski, P., Bataillon, T., Ettema, T.J.G., Jochum, L.M., Schreiber, L., Chen, X., Lever, M.A., Polz, M.F., Jørgensen, B.B., Schramm, A., et al. (2017). Microbial community assembly and evolution in subseafloor sediment. Proc. Natl. Acad. Sci. USA *114*, 2940–2945. https://doi.org/10.1073/pnas.1614190114.

41. Shimabukuro, M., Zeppilli, D., Leduc, D., Wenzhöfer, F., Berg, P., Rowden, A.A., and Glud, R.N. (2022). Intra- and inter-spatial variability of meiofauna in hadal trenches is linked to microbial activity and food availability. Sci. Rep. *12*, 4338. https://doi.org/10.1038/s41598-022-08088-1.

42. Nunoura, T., Hirai, M., Yoshida-Takashima, Y., Nishizawa, M., Kawagucci, S., Yokokawa, T., Miyazaki, J., Koide, O., Makita, H., Takaki, Y., et al. (2016). Distribution and Niche Separation of Planktonic Microbial Communities in the Water Columns from the Surface to the Hadal Waters of the Japan Trench under the Eutrophic Ocean. Front. Microbiol. *7*, 1261. https://doi.org/10.3389/fmicb.2016.01261.

43. Zhu, G., Yang, H., Lin, J., Zhou, Z., Xu, M., Sun, J., and Wan, K. (2019). Along-strike variation in slab geometry at the southern Mariana subduction zone revealed by seismicity through ocean bottom seismic experiments. Geophys. J. Int. *218*, 2122–2135. https://doi.org/10.1093/gji/ggz272.

44. Jiang, H., Xin, X., Xu, H., Zhou, C., Vetter, P.A., Yu, L., Long, T., Chen, Q., and Tian, J. (2024). Three-layer circulation in the world deepest hadal trench. Nat. Commun. *15*, 8949. https://doi.org/10.1038/s41467-024-53370-7.

45. Parks, D.H., Chuvochina, M., Rinke, C., Mussig, A.J., Chaumeil, P.-A., and Hugenholtz, P. (2022). GTDB: an ongoing census of bacterial and archaeal diversity through a phylogenetically consistent, rank normalized and complete genome-based taxonomy. Nucleic Acids Res. *50*, D785–D794. https://doi.org/10.1093/nar/gkab776.

46. R Core Team (2025). R: a Language and Environment for Statistical Computing (R Foundation for Statistical Computing).

47. Parnell, A. (2021). Simmr: A Stable Isotope Mixing Model. https://doi.org/10.32614/CRAN.package.simmr.

48. Stekhoven, D.J., and Bühlmann, P. (2012). MissForest—non-parametric missing value imputation for mixed-type data. Bioinformatics *28*, 112–118. https://doi.org/10.1093/bioinformatics/btr597.

49. Oksanen, J., Blanchet, F.G., Friendly, M., Kindt, R., Legendre, P., McGlinn, D., Minchin, P.R., O'Hara, R.B., Simpson, G.L., Solymos, P., et al. (2020). Vegan: Community Ecology Package. https://doi.org/10.32614/CRAN.package.vegan.

50. Hijmans, R.J. (2022). Raster: Geographic Data Analysis and Modeling. https://doi.org/10.32614/CRAN.package.raster.

51. Morgan-Wall, T. (2023). Rayshader: Create Maps and Visualize Data in 2D and 3D. https://doi.org/10.32614/CRAN.package.rayshader.

52. Li, D., Liu, C.-M., Luo, R., Sadakane, K., and Lam, T.-W. (2015). MEGAHIT: an ultra-fast single-node solution for large and complex metagenomics assembly via succinct de Bruijn graph. Bioinformatics *31*, 1674–1676. https://doi.org/10.1093/bioinformatics/btv033.

53. Li, H., and Durbin, R. (2009). Fast and accurate short read alignment with Burrows-Wheeler transform. Bioinformatics *25*, 1754–1760. https://doi.org/10.1093/bioinformatics/btp324.

54. Kang, D.D., Li, F., Kirton, E., Thomas, A., Egan, R., An, H., and Wang, Z. (2019). MetaBAT 2: An adaptive binning algorithm for robust and efficient genome reconstruction from metagenome assemblies. PeerJ *7*, e7359. https://doi.org/10.7717/peerj.7359.

55. Aroney, S.T.N., Newell, R.J.P., Nissen, J.N., Camargo, A.P., Tyson, G.W., and Woodcroft, B.J. (2025). CoverM: read alignment statistics for metagenomics. Bioinformatics *41*, btaf147. https://doi.org/10.1093/bioinformatics/btaf147.

56. Hyatt, D., Chen, G.-L., Locascio, P.F., Land, M.L., Larimer, F.W., and Hauser, L.J. (2010). Prodigal: prokaryotic gene recognition and translation initiation site identification. BMC Bioinform. *11*, 119. https://doi.org/10.1186/1471-2105-11-119.

57. Queirós, P., Delogu, F., Hickl, O., May, P., and Wilmes, P. (2021). Mantis: flexible and consensus-driven genome annotation. GigaScience *10*, giab042. https://doi.org/10.1093/gigascience/giab042.

58. Wickham, H., Averick, M., Bryan, J., Chang, W., McGowan, L.D., François, R., Grolemund, G., Hayes, A., Henry, L., Hester, J., et al. (2019). Welcome to the tidyverse. J. Open Source Softw. *4*, 1686. https://doi.org/10.21105/joss.01686.

59. Wickham, H. (2016). ggplot2: Elegant Graphics for Data Analysis (Springer-Verlag New York).

60. Baselga, A., Orme, D., Villeger, S., De Bortoli, J., Leprieur, F., Logez, M., Martinez-Santalla, S., Martin-Devasa, R., Gomez-Rodriguez, C., and Crujeiras, R.M. (2023). Betapart: Partitioning Beta Diversity into Turnover and Nestedness Components. https://doi.org/10.32614/CRAN.package.betapart.

61. Watts, S.C., Ritchie, S.C., Inouye, M., and Holt, K.E. (2019). FastSpar: rapid and scalable correlation estimation for compositional data. Bioinformatics *35*, 1064–1066. https://doi.org/10.1093/bioinformatics/bty734.

62. Friedman, J., and Alm, E.J. (2012). Inferring Correlation Networks from Genomic Survey Data. PLOS Comput. Biol. *8*, e1002687. https://doi.org/10.1371/journal.pcbi.1002687.

63. Bastian, M., Heymann, S., and Jacomy, M. (2009). Gephi: An Open Source Software for Exploring and Manipulating Networks. ICWSM *3*, 361–362. https://doi.org/10.1609/icwsm.v3i1.13937.

64. Csárdi, G., Nepusz, T., Traag, V., Horvát, S., Zanini, F., Noom, D., Müller, K., Schoch, D., and Salmon, M. (2026). Igraph: Network Analysis and Visualization in R. https://doi.org/10.5281/zenodo.7682609.

65. Yu, F., Haynes, S.E., Teo, G.C., Avtonomov, D.M., Polasky, D.A., and Nesvizhskii, A.I. (2020). Fast Quantitative Analysis of timsTOF PASEF

Data with MSFragger and IonQuant. Mol. Cell. Proteomics *19*, 1575–1585. https://doi.org/10.1074/mcp.tir120.002048.

66. Kong, A.T., Leprevost, F.V., Avtonomov, D.M., Mellacheruvu, D., and Nesvizhskii, A.I. (2017). MSFragger: ultrafast and comprehensive peptide identification in mass spectrometry–based proteomics. Nat. Methods *14*, 513–520. https://doi.org/10.1038/nmeth.4256.
67. Da Veiga Leprevost, F., Haynes, S.E., Avtonomov, D.M., Chang, H.-Y., Shanmugam, A.K., Mellacheruvu, D., Kong, A.T., and Nesvizhskii, A.I. (2020). Philosopher: a versatile toolkit for shotgun proteomics data analysis. Nat. Methods *17*, 869–870. https://doi.org/10.1038/s41592-020-0912-y.
68. Yang K.L., Yu, F., Teo, G.C., Li, K., Demichev, V., Ralser, M., and Nesvizhskii, A.I. (2023). MSBooster: improving peptide identification rates using deep learning-based features. Nat. Commun. *14*, 4539. https://doi.org/10.1038/s41467-023-40129-9.
69. The, M., MacCoss, M.J., Noble, W.S., and Käll, L. (2016). Fast and Accurate Protein False Discovery Rates on Large-Scale Proteomics Data Sets with Percolator 3.0. J. Am. Soc. Mass Spectrom. *27*, 1719–1727. https://doi.org/10.1007/s13361-016-1460-7.
70. Nesvizhskii, A.I., Keller, A., Kolker, E., and Aebersold, R. (2003). A Statistical Model for Identifying Proteins by Tandem Mass Spectrometry. Anal. Chem. *75*, 4646–4658. https://doi.org/10.1021/ac0341261.
71. Yu, F., Haynes, S.E., and Nesvizhskii, A.I. (2021). IonQuant Enables Accurate and Sensitive Label-Free Quantification With FDR-Controlled Match-Between-Runs. Mol. Cell. Proteomics *20*, 100077. https://doi.org/10.1016/j.mcpro.2021.100077.
72. Sjoberg, D. (2025) Ggsankey: Sankey, Alluvial and Sankey Bump Plots.
73. Soetaert, K., and Petzoldt, T. (2020). Marelac: Tools for Aquatic Sciences. https://doi.org/10.32614/CRAN.package.marelac.
74. Soetaert, K., and Meysman, F. (2012). Reactive transport in aquatic ecosystems: Rapid model prototyping in the open source software R. Environ. Modell. Softw. *32*, 49–60. https://doi.org/10.1016/j.envsoft.2011.08.011.
75. Luo, F., Zhong, J., Yang, Y., Scheuermann, R.H., and Zhou, J. (2006). Application of random matrix theory to biological networks. Phys. Lett. A *357*, 420–423. https://doi.org/10.1016/j.physleta.2006.04.076.
76. Deng, Y., Jiang, Y.-H., Yang, Y., He, Z., Luo, F., and Zhou, J. (2012). Molecular ecological network analyses. BMC Bioinform. *13*, 113. https://doi.org/10.1186/1471-2105-13-113.
77. Jacomy, M., Venturini, T., Heymann, S., and Bastian, M. (2014). ForceAtlas2, a Continuous Graph Layout Algorithm for Handy Network Visualization Designed for the Gephi Software. PLOS One *9*, e98679. https://doi.org/10.1371/journal.pone.0098679.
78. Niu, M., Fan, X., Zhuang, G., Liang, Q., and Wang, F. (2017). Methane-metabolizing microbial communities in sediments of the Haima cold seep area, northwest slope of the South China Sea. FEMS Microbiol. Ecol. *93*. https://doi.org/10.1093/femsec/fix101.
79. Briscoe, L., Halperin, E., and Garud, N.R. (2023). SNV-FEAST: microbial source tracking with single nucleotide variants. Genome Biol. *24*, 101. https://doi.org/10.1186/s13059-023-02927-8.
80. Knights, D., Kuczynski, J., Charlson, E.S., Zaneveld, J., Mozer, M.C., Collman, R.G., Bushman, F.D., Knight, R., and Kelley, S.T. (2011). Bayesian community-wide culture-independent microbial source tracking. Nat. Methods *8*, 761–763. https://doi.org/10.1038/nmeth.1650.
81. Zhao, R., Mogollón, J.M., Abby, S.S., Schleper, C., Biddle, J.F., Roerdink, D.L., Thorseth, I.H., and Jørgensen, S.L. (2020). Geochemical transition zone powering microbial growth in subsurface sediments. Proc. Natl. Acad. Sci. USA *117*, 32617–32626. https://doi.org/10.1073/pnas.2005917117.
82. Akbarzadeh, Z., Laverman, A.M., Rezanezhad, F., Raimonet, M., Viollier, E., Shafei, B., and Van Cappellen, P. (2018). Benthic nitrite exchanges in the Seine River (France): An early diagenetic modeling analysis. Sci. Total Environ. *628–629*, 580–593. https://doi.org/10.1016/j.scitotenv.2018.01.319.
83. Berg, C., Listmann, L., Vandieken, V., Vogts, A., and Jürgens, K. (2015). Chemoautotrophic growth of ammonia-oxidizing Thaumarchaeota enriched from a pelagic redox gradient in the Baltic Sea. Front. Microbiol. *5*, 786. https://doi.org/10.3389/fmicb.2014.00786.
84. Zhang, Y., Qin, W., Hou, L., Zakem, E.J., Wan, X., Zhao, Z., Liu, L., Hunt, K.A., Jiao, N., Kao, S.-J., et al. (2020). Nitrifier adaptation to low energy flux controls inventory of reduced nitrogen in the dark ocean. Proc. Natl. Acad. Sci. USA *117*, 4823–4830. https://doi.org/10.1073/pnas.1912367117.
85. Canavan, R.W., Laverman, A.M., and Slomp, C.P. (2007). Modeling nitrogen cycling in a coastal fresh water sediment. Hydrobiologia *584*, 27–36. https://doi.org/10.1007/s10750-007-0583-z.
86. Westrich, J.T., and Berner, R.A. (1984). The role of sedimentary organic matter in bacterial sulfate reduction: The G model tested1. Limnol. Oceanogr. *29*, 236–249. https://doi.org/10.4319/lo.1984.29.2.0236.
87. Redfield, A.C. (1934) On the Proportions of Organic Derivatives in Sea Water and Their Relation to the Composition of Plankton (University Press of Liverpool Liverpool).
88. Volz, J.B., Mogollón, J.M., Geibert, W., Arbizu, P.M., Koschinsky, A., and Kasten, S. (2018). Natural spatial variability of depositional conditions, biogeochemical processes and element fluxes in sediments of the eastern Clarion-Clipperton Zone, Pacific Ocean. Deep Sea Res. I *140*, 159–172. https://doi.org/10.1016/j.dsr.2018.08.006.
89. Christensen, E.R. (1982). A model for radionuclides in sediments influenced by mixing and compaction. J. Geophys. Res. *87*, 566–572. https://doi.org/10.1029/JC087iC01p00566.
90. Boudreau, B.P. (1997) Diagenetic Models and Their Implementation: Modelling Transport and Reactions in Aquatic Sediments (Springer Berlin Heidelberg).
91. Benjamini, Y., and Hochberg, Y. (1995). Controlling the False Discovery Rate: A Practical and Powerful Approach to Multiple Testing. J. R. Stat. Soc. B *57*, 289–300. https://doi.org/10.1111/j.2517-6161.1995.tb02031.x.

STAR★METHODS

KEY RESOURCES TABLE

REAGENT or RESOURCE	SOURCE	IDENTIFIER
Chemicals, peptides, and recombinant proteins		
1 M Tris-HCl, pH 8.0	Thermo Fisher Scientific	cat#15568025
10% SDS solution	Invitrogen	cat#15553027
Ethanol	Sangon Biotech	cat#A500737-0500
Methanol	Macklin	cat#M813904-4L
Nuclease-free water	Invitrogen	cat#AM9937
Protease &Phosohatase Inhibitor single-Use Cocktail	Thermo Scientific	cat#1861280
Tris-saturated phenol, pH 7.7–8.1	Macklin	cat#T917981-200ml
Trypsin/Lys-C	Promega	cat#V5073
Ammonium acetate	Macklin	cat#A801001-500g
Dithiothreitol (DTT)	Aladdin	cat#D104859-25g
EDTA-Na2	Solarbio	cat#E8030
Sucrose	Macklin	cat#S6212-500g
Urea	Macklin	cat#U6209-500g
Critical commercial assays		
PowerUp SYBR Green Master Mix	Applied Biosystems	cat#01145665
Deposited data		
Metagenomic data	Xiao et al.[20]	https://www.biosino.org/node/project/detail/OEP004067
Metaproteomic data	This study	iProX (https://www.iprox.cn/): PXD065548
GTDB database release 220	Parks et al.[45]	https://gtdb.ecogenomic.org/
The common repository of adventitious proteins	The Global Proteome Machine Organization	https://www.thegpm.org/crap/
Oligonucleotides		
Bacterial 16S rRNA gene primer set bac341f CCTACGGGWGGCWGCA	Sangon Biotech	N/A
Bacterial 16S rRNA gene primer set 519r TTACCGCGGCKGCTG	Sangon Biotech	N/A
Archaeal 16S rRNA gene primer set Uni519f CAGCMGCCGCGGTAA	Sangon Biotech	N/A
Archaeal 16S rRNA gene primer set Arc908R CCCGCCAATTCCTTTAAGTT	Sangon Biotech	N/A
Software and algorithms		
ProPopMove (v0.5.2)	This study	https://github.com/zhenjiaofenjie/ProPopMove
R (v4.5.2)	R Core Team[46]	https://cran.r-project.org/
simmr (v0.5.1.212)	Parnell[47]	https://CRAN.R-project.org/package=simmr
missForest (v1.6.1)	Stekhoven[48]	https://CRAN.R-project.org/package=missForest
vegan (v2.6.4)	Oksanen et al.[49]	https://CRAN.R-project.org/package=vegan
raster (v3.6.23)	Hijmans[50]	https://CRAN.R-project.org/package=raster
rayshader (v0.35.7)	Morgan-Wall[51]	https://CRAN.R-project.org/package=rayshader

(*Continued on next page*)

Continued

REAGENT or RESOURCE	SOURCE	IDENTIFIER
MEGAHIT (v1.2.9)	Li et al.[52]	https://github.com/voutcn/megahit
BWA-MEM (v0.7.17-r1188)	Li and Durbin[53]	https://github.com/lh3/bwa
MetaBAT2 (v2.12.1)	Kang et al.[54]	https://bitbucket.org/berkeleylab/metabat
dRep (v3.4.0)	Olm et al.[31]	https://github.com/MrOlm/drep
coverM (v0.7.0)	Aroney et al.[55]	https://github.com/wwood/CoverM
Prodigal (v2.6.3)	Hyatt et al.[56]	https://github.com/hyattpd/Prodigal
Mantis (v1.5.5)	Queirós et al.[57]	https://github.com/PedroMTQ/mantis
tidyverse (v1.3.1)	Wickham et al.[58]	https://CRAN.R-project.org/package=tidyverse
ggplot2 (v3.3.5)	Wickham[59]	https://CRAN.R-project.org/package=ggplot2
betapart (v1.6.0)	Baselga et al.[60]	https://CRAN.R-project.org/package=betapart
FastSpar (v1.0.0)	Watts et al.,[61] Friedman et al.[62]	https://github.com/scwatts/fastspar
Gephi (v0.10.1)	Bastian et al.[63]	https://gephi.org/
igraph (v1.5.0.1)	Csardi and Nepusz[64]	https://CRAN.R-project.org/package=betapart
Fragpipe platform (v18.0)	Yu et al.[65]	https://fragpipe.nesvilab.org
MSFragger (v3.5)	Kong et al.[66]	https://msfragger.nesvilab.org
Philosopher (v4.4.0)	Da Veiga Leprevost et al.[67]	https://philosopher.nesvilab.org
MSBooster (v1.1.4)	Demichev et al.[68]	https://github.com/Nesvilab/MSBooster
Percolator (v3.0.5)	The et al.[69]	https://github.com/percolator/percolator/
ProteinProphet (v4.4.0)	Nesvizhskii et al.[70]	https://proteinprophet.sourceforge.net
IonQuant (v1.8.0)	Yu et al.[71]	http://ionquant.nesvilab.org
ggsankey (v0.0.99999)	Sjoberg[72]	https://github.com/davidsjoberg/ggsankey
marelac (v2.1.11)	Soetaert and Petzoldt[73]	https://CRAN.R-project.org/package=marelac
ReacTran (v1.4.3.1)	Soetaert and Meysman[74]	https://CRAN.R-project.org/package=ReacTran
DEoptim (v2.2.6)	Ardia et al.[34]	https://CRAN.R-project.org/package=DEoptim
Other		
Data and code to reproduce the results in this work	This study	https://scidata.sjtu.edu.cn/records/tqazd-was05

EXPERIMENTAL MODEL AND STUDY PARTICIPANT DETAILS

No experimental models nor human participants were included in this study. Samples used in this study were directly collected from natural oceanic environments using the HOV Fendouzhe and equipment onboard. No culturing of microbe strains, cell lines, nor primary cell cultures has been conducted.

METHOD DETAILS

Geochemical measurements and analyses

Dissolved oxygen concentrations were measured on deck using a high-performance oxygen microsensor (Unisense, Denmark). The remaining geochemical measurements were conducted at the Instrumental Analysis Centre of Shanghai Jiao Tong University, Shanghai, China. The organic carbon concentration and the corresponding isotopic values were determined by an elemental analyzer (Vario EL III, Elementar, Germany) coupled with an isotope ratio mass spectrometer (Isoprime, Elementar, Germany). The isotopic values were reported relative to the Vienna-Pee Dee Belemnite (V-PDB) standard. Porewater was extracted by centrifuging at 10 000 × g at 4 °C for 30 min. The supernatants were then filtered through a 0.22 μm membrane. The concentrations of nitrate, nitrite, ammonium, and sulfate in the porewater were analyzed by ion chromatography ICS-5000+/900 (Thermo Scientific Dionex™,

United States of America). To avoid interference between porewater extraction and solid-phase analyses, porewater geochemistry and solid-phase geochemistry were measured on separate replicate sediment cores from the same station, and the results were merged by matching corresponding sediment depth intervals.

Samples with >40% missing geochemical parameters were excluded. Parameters with missing values in >35% of the remaining samples were also removed; this filtering step excluded δ^{13}C-DIC and DIC. The retained geochemical data were used for direct visualization and input into biogeochemical reactive-transport modeling. A stable isotope mixing model from the R package simmr (v0.5.1.212)[47] was used to estimate the source of organic carbon in sediment samples. For correlation analyses between geochemical parameters and multi-omics data, remaining missing values were imputed using the R package missForest (v1.6.1),[48] and all parameters were standardized (zero-mean, unit-variance) to remove scale effects. Redundancy analysis (RDA) was then performed using R package vegan (v2.6.4)[49] on the standardized geochemical dataset to assess the relative contributions of water depth, sediment depth, and TPI to geochemical variation.

Topographic data analysis and modeling

The bathymetric map was obtained from multibeam sonar measurements. The resolution of the map was 110 m. Data analysis and modeling were performed using the R package raster (v3.6.23).[50] The 3D bathymetric plots were constructed by the R package rayshader (v0.35.7).[51] The TPI value for each cell on the map was calculated by comparing the water depth of that cell to the mean value of its neighboring cells in a 100 $\times$ 100-cell ''moving window''. We tested several neighborhood sizes for the ''moving window'' surrounding each cell and determined that a size of 100 $\times$ 100 cells was the most appropriate for quantifying the topographic features in this study.

Metagenomic analyses

Sample collection, DNA extraction, and metagenomic sequencing were described in the previous MEER study.[20] In brief, sediment samples were collected using HOV *Fendouzhe* via push cores and sliced at $\sim$2 cm intervals. Microbial DNA was extracted from 0.5 g sediment samples using MGIEasy Environmental Microbiome DNA Extraction Kits (MGI-Tech, China), with multiple extractions combined for low-yield samples. Sequencing libraries were prepared using MGIEasy Fast FS DNA Library Prep Sets and sequenced on DNBSEQ-T series machines to generate 150 bp paired-end reads. Clean reads were assembled into contigs using MEGAHIT (v1.2.9).[52] Samples were randomly grouped into sets of $\sim$100 samples each. In each sample set, clean reads from all samples were individually mapped against the contigs of each sample using BWA-MEM (v0.7.17-r1188),[53] generating within- and between-sample coverage matrices for each contig. Contigs were binned sample-by-sample using MetaBAT2 (v2.12.1)[54] based on these coverage matrices. Metagenome-assembled genomes (MAGs) with $\geq$50% completeness and $\leq$10% contamination were dereplicated using dRep (v3.4.0),[31] at 95% ANI thresholds to obtain 7,564 species-resolved genomes (SRGs). SRG relative abundances were calculated using coverM (v0.7.0) with the relative abundance and RPKM methods,[55] and taxonomic annotation was performed against the GTDB database release 220.[45] Genes in SRGs were predicted with Prodigal (v2.6.3)[56] and annotated using Mantis (v1.5.5)[57] to obtain KEGG ortholog information.

Community diversity analyses

We applied a minimum mapping threshold of 30% coverage per sample to ensure accurate representation of microbial diversity using SRG abundances. Among topography-targeted trench bottom and abyssal samples, 7,346 SRGs were detected with an average mapping rate of 74.4%. When expanded to include all trench bottom and abyssal samples, 7,458 SRGs were detected with an average mapping rate of 72.0%. At the trench slope, 6,692 SRGs were detected with an average mapping rate of 69.3% in fault zone samples, while 7,403 SRGs were detected with an average mapping rate of 68.0% across all slope samples, indicating robust genome recovery across topographically diverse sites.

Alpha diversity (community member diversity within each sample) and beta diversity (community composition dissimilarity between samples) were calculated based on the abundance distribution of SRGs using the R package vegan (v2.6.4).[49] Data manipulation and visualization were then completed using the tidyverse (v1.3.1) and ggplot2 (v3.3.5) R packages.[58,59] Beta diversity indices were partitioned into species loss and species replacement components by using the R package betapart (v1.6.0).[60]

Co-occurrence networks were constructed for prevalent SRGs (detected in at least 30% of samples within each topographic group) using FastSpar (v1.0.0).[61,62] Correlation thresholds were determined based on the topological structure of the networks using Random Matrix Theory (RMT).[75,76] Briefly, for a range of candidate thresholds (0.5–0.9, step = 0.1), the correlation matrix was filtered at each threshold, eigenvalues of the resulting adjacency matrix were computed, and the nearest-neighbor spacing distribution (NNSD) of the unfolded eigenvalues was compared to the theoretical Gaussian Orthogonal Ensemble (GOE, Wigner–Dyson distribution) and Poisson distributions using chi-square statistics. The optimal threshold was identified at the transition point where the chi-square statistic for the GOE distribution began to increase while the Poisson chi-square remained stable, indicating the shift from non-random to random network structure. This procedure yielded a correlation threshold of 0.7 across all three topographic groups. Networks were visualized in Gephi (v0.10.1)[63] using the ForceAtlas2 layout algorithm,[77] with edge weights defined as 1.2 + correlation. Network-level centrality metrics (betweenness, closeness, degree, and eigenvector centrality) and density were calculated using the R package igraph (v1.5.0.1).[64]

Microbial biomass quantification based on 16S rRNA gene copy numbers

Real-time qPCR experiments were performed on an Applied Biosystems QuantStudio 3 Real-Time PCR System (Applied Biosystems, MA, USA). Bacterial 16S rRNA genes were quantified using primer set bac341f (5′-CCTACGGGWGGCWGCA-3′) and 519r (5′-TTACCGCGGCKGCTG-3′).[78] Archaeal 16S rRNA genes were quantified using primer set Uni519f (5′-CAGCMGCCGCGGTAA-3′) and Arc908R (5′-CCCGCCAATTCCTTTAAGTT-3′).[78] For bacterial 16S rRNA gene quantification, the 20 μL reaction mixture contained: 10 μL PowerUp SYBR Green Master Mix (Applied Biosystems, MA, USA), 1.3 μL each of 10 μM forward and reverse primers (Sangon Biotech, Shanghai, China), 2 μL template DNA, and autoclaved double-distilled water to 20 μL final volume. The thermal cycling program consisted of initial denaturation at 95°C for 15 min, followed by 40 cycles of 95°C for 30 s, 56°C for 30 s, 72°C for 30 s, and 79°C for 15 s. For archaeal 16S rRNA gene quantification, the 20 μL reaction mixture contained identical components with the following thermal cycling program: initial denaturation at 95°C for 15 min, followed by 40 cycles of 95°C for 30 s, 60°C for 30 s, 72°C for 30 s, and 80°C for 15 s. Standard curves were generated for each gene target, with all reactions achieving $R^2 > 0.99$ and amplification efficiencies between 90-110%.

Protein extraction

In general, 2g of thoroughly mixed sediment sample was used for coextraction of DNA and protein. 2g of sediment sample, a gram quartz sand (~1 mm diameter), 1 mL sodium dodecyl sulfate (SDS) buffer (1% SDS, 240 mM sodium phosphate buffer (pH 8.0), 20 mM sodium EDTA, 40 mM dithiothreitol (DTT), 60% sucrose), 2 mL phenol (Tris saturated phenol, pH 7.7-8.1, containing 0.1% 8-hydroxyquinoline), and 30 μL protease inhibitor (HaltTM Protease and Phosphatase Inhibitor Single-Use Cocktail, Thermo Scientific) were added into 15 mL sterile polypropylene centrifuge tubes. Then, the samples were homogenized (4 m/s, 20 s) three times (3 min intervals) with a homogenizer (FastPrep-24, MP Biomedical). After grinding, the tubes were centrifuged (10,000 ×g, 5 min) at 4 °C.

The upper organic phase was transferred to a new 15 mL centrifuge tube, mixed by inversion with five times the volume of methanol-ammonium acetate (0.1 M ammonium acetate dissolved in methanol), and centrifuged (10,000 ×g, 10 min) after 16 hours of incubation at -20 °C. And the supernatant was removed carefully to avoid the protein loss. The pellet of protein was washed with pre-cooled anhydrous ethanol. After suspension in 1 mL anhydrous ethanol, the precipitate was transferred to a 1.5 mL centrifuge tube and centrifuged (14,000 ×g, 5 min) at 4°C. The protein precipitate was air-dried and finally dissolved in 40 μL of 8 M urea (8 M urea dissolved in 0.1 M Tris-HCl, pH 8.0). The extracted protein solution was used immediately for digestion and purification or stored at -70 °C for subsequent experiments.

Enzymatic cleavage of proteins and purification of peptides

In general, 1-10 μg of protein was diluted to 50 μL with 8 M urea. The protein solution was mixed with 2 μL of 0.5 M DTT (0.5 M DTT dissolved in 8 M urea) and incubated at 37 °C for 30 min. Then, the sample was mixed with 5 μL of 0.5 M IAA (0.5 M IAA dissolved in 8 M urea) and incubated for 30 min at room temperature while being protected from light, followed by mixing with 2 μL of 0.5 M DTT. The alkylated protein was combined with 413 μL of 50 mM ammonium bicarbonate buffer (50 mM ammonium bicarbonate dissolved in water), mixed at a ratio 1:25 (by protein mass) with trypsin/lysine endonuclease (Trypsin/Lys-C Mix, mass spectrometry grade, Promega), and incubated for 16 hours at 37 °C. The digested sample was filtered using a 0.5 mL 10 kDa ultrafiltration filter (Microcon-10 kDa, Millipore) by centrifugation (12,000 ×g, 40 min), and the filtrate was collected. Then the filtrate was gently dried in a centrifugal concentrator and peptides could be analyzed immediately using nLC-ESI-MS/MS for shotgun proteomics or stored at -70 °C.

Mass spectrometry data acquisition

Based on the concentrations determined by Nanodrop, 8 μL of peptide solution was used per injection in the nLC–MS/MS system comprised of a nanoElute® liquid chromatography instrument (Bruker) and timsTOF Pro mass spectrometry instrument (Bruker). Peptides were separated on a reversed-phase C18 analytical column (25 cm × 75 μm ID, APT) with an overall gradient from 2% to 95% acetonitrile at a flow rate of 300 nL/min over 90 min at 60 °C. Data-dependent acquisition (DDA) was performed in PASEF mode (oTOF control v6.0.0.12). The ion mobility window was set to 1/k0 start = 0.6 Vs/cm^2 to 1/k0 end = 1.6 Vs/cm^2, with a ramp time of 100 ms with a locked duty cycle and a mass range of 100-1,700 m/z. MS/MS spectra were acquired with an accumulation time of 2 ms and a cycle time of 100 ms. The target intensity was set at 6,000, and the threshold intensity was set at 200.

Metaproteomic searching, peptide validation, protein inference and quantification

Raw DDA files from three replicate injections of peptides acquired on a timsTOF Pro mass spectrometer (Bruker) were used. The Fragpipe platform (v18.0)[65] with MSFragger (v3.5)[65,66] and Philosopher (v4.4.0)[67] were used to perform decoy generation, searching, peptide validation, and protein inference. Predicted genes from all SRGs were used as reference database for protein inference, minimizing the false positive rates compared to using public non-hadal databases. Reversed protein sequences were appended to the original databases as decoys for MSFragger. The common repository of adventitious proteins (cRAP, https://www.thegpm.org/crap/) was used as the contaminant proteins. For the two-step database search, the initial search was performed with both precursor and fragment mass tolerances set to 40 ppm. Tryptic cleavage specificity was applied, and up to two missed trypsin cleavages were allowed. Isotope error was set to 0/1/2. Peptides with 7-50 amino acids and 500-5,000 Da were considered for identification. The search included variable methionine oxidation, variable protein N-terminal acetylation, and fixed carbamidomethyl cysteine modifications. The maximum number of variable modifications per peptide was set to 3. The peptide-spectrum matches (PSMs) were

further rescored using deep learning prediction by the MSBooster (v1.1.4)[68] module, and discrimination between correct and decoy spectra was performed by Percolator (v3.0.5).[69] The validated peptides were assigned either as unique peptides to a particular protein or as razor peptides to a single protein that had the most peptide evidence by ProteinProphet (v4.4.0).[70] The results of the first step, including peptides and proteins, were filtered with a 25% false discovery rate (FDR). For the second step of the search, the inferred proteins generated from the first search were used as the database and then subjected to the same parameters, except they were filtered with a 1% FDR. The MaxLFQ intensity, including unique and razor peptides, was calculated using IonQuant (v1.8.0)[71] with a 1% match between run ion FDR and one MaxLFQ min ion. Proteins that had at least three unique peptide count were retained. Activities of SRGs were determined as the total peptide counts of proteins belong to each SRG in each sample. Sankey pump plots showing the SRG activity along with sediment depths were produced using R package ggsankey (v0.0.99999).[72]

Estimations of microbial population dispersal

An R package ProPopMove (https://github.com/zhenjiaofenjie/ProPopMove) was developed to estimate the net microbial population movement between samples. The estimation of microbial dispersal dynamics was built upon two principles: defining the movement of microorganisms, and inferring the directional movement between microbial communities. Unlike previous source tracking methods that rely on identical 16S rRNA gene amplicons or single nucleotide variants (SNVs) shared between artificially designated sources and sinks,[79,80] this approach here reconstructs microbial dispersal patterns and their directionality by analyzing species-level microdiversities based on metagenome assembled genomes. As a species moves from its source to various destinations, it undergoes both random and environmental selective mutations (Figure 5**A**). Consequently, upon sequencing, assembling, and binning these microbial communities separately, we obtain a series of similar-but-not-identical genomes corresponding to the same microbial species within a circle of 95% ANI. The genome that maintains high similarity with all other genomes is then picked as the SRG, which is most likely to represent the initial genome from which all mutants originated. Therefore, potential movement paths are reconstructed from the SRG's source sample to all other sink samples that contain this species (Figures 5**A and 5B**). Movement between microbial communities was then inferred based on all the species-level movements between them (Equation 1), which helps mitigate the influence of random noise that may affect the observed movement of a single species. The net flux of microbial movement between samples A and B was defined as:

$$F_{AB} = \frac{\sum_{i}^{n} R_{AB,i}}{n} - \frac{\sum_{j}^{m} R_{BA,j}}{m} \quad \text{(Equation 3)}$$

where n is the number of SRGs originating from sample A, $R_{AB,i}$ is the relative abundance of the i-th SRG (originating from A) in sample B, m is the number of SRGs originating from sample B, and $R_{BA,j}$ is the relative abundance of the j-th SRG (originating from B) in sample A. The magnitude of dispersal is represented by the absolute value of F_{AB}, while its sign indicates movement direction (positive values indicate movement from A to B, negative values indicate the opposite). Sample pair order was adjusted to ensure F remained positive, such that:

$$F = f_{forward} - f_{reverse} \quad \text{(Equation 4)}$$

Sample pairs with F values approaching zero could indicate either isolation (e.g., distant sediment samples) or balanced bidirectional exchange (e.g., adjacent samples). These scenarios were distinguished by further examining $f_{forward}$ and $f_{reverse}$ values.

Rather than applying arbitrary cutoffs on fluxes, we employed a bootstrapping approach (n = 9999) on SRG-sample assignments to generate null distributions of F, $f_{forward}$, and $f_{reverse}$ values. The proportional ranking (scaled 0-1) of observed values compared to these null distributions was calculated and adjusted for multiple comparisons using the FDR method. Sample pairs were classified as: A) "Isolated" when the adjusted proportional ranking of $f_{forward}$ was below 0.1; B) "Transmit" when the adjusted proportional ranking of F exceeded 0.9 and pairs were not "Isolated"; C) "Mixed" when the adjusted proportional ranking of $f_{reverse}$ exceeded 0.9 and pairs were not "Transmit." Remaining pairs indistinguishable from bootstrapping results were classified as "Others."

Biogeochemical modeling

A 1-D reactive-transport model was used to simulate biogeochemical processes in the sediments[81,82]:

$$\frac{d(\varphi C)}{dt} = \frac{d}{dx}\left(\varphi D_s \frac{dC}{dx}\right) - \frac{d(\varphi \vartheta C)}{dx} + R_{net} \quad \text{(Equation 5)}$$

where

C: the compound concentration
φ: the sediment porosity
D_s: the diffusion coefficient of the compound
ϑ: the velocity

R_{net}: the combined net flux of all microbially-mediated reactions related to this compound.

In the model, all geochemical compounds were assumed to be at a steady state, i.e., the combined effects of sedimentation, diffusion, and microbial activities kept their concentrations constant[81,82]:

$$\frac{d(\varphi C)}{dt} = 0 \quad \text{(Equation 6)}$$

Therefore, the net rates of microbially-mediated reactions could be estimated based on the measured geochemical profiles:

$$R_{net} = -\frac{d}{dx}\left(\varphi D_s \frac{dC}{dx}\right) + \frac{d(\varphi \vartheta C)}{dx} \quad \text{(Equation 7)}$$

The individual reaction rates comprising the same net flux were further estimated based on Michaelis-Menten kinetic kinetics. The benthic microbial reaction activities were summarized as 11 primary and three secondary reactions in the model based on reports in a published study[81] (Figure 6A; Table S4). The primary reactions included aerobic respiration, nitrite oxidation, aerobic Mn oxidation, sulfide oxidation, dissimilatory Mn reduction, nitrate reduction to nitrite, denitrification from nitrite, dissimilatory nitrate reduction to ammonium (DNRA) from nitrite, anaerobic ammonium oxidation (anammox), nitrification, sulfate reduction. Secondary reactions represented the carbon fixation processes that related to anammox, nitrification, and nitrite oxidation. The carbon fixation efficiencies were adopted from references[83,84] (Table S4). We did not consider the carbon fixation contributions of Mn and sulfide oxidation because the carbon fixation efficiencies of these two reactions are largely unknown. To make the reaction rates comparable to each other, we rescaled the reaction stoichiometries to transfer four electrons per reaction, equal to the redox equivalent required to oxidize one atom of organic carbon or fix one atom of inorganic carbon (Table S4).

Model parameters are shown in Tables S5 and S6. A 3-G method was used to define the TOC pool, wherein TOC1, TOC2, and TOC3 represent the labile, semi-labile, and refractory organic matter.[82,85,86] The fractions of TOC contents were calibrated during modeling. The C/N ratio of the whole OM pool was assumed to follow the Redfield ratio.[87,88] The distribution of bioturbation intensity with depth was described using a Gaussian-type function.[89] Sediment porosity was assumed to follow an exponentially decreasing trend. The surface porosity (0.83) was obtained from literature,[14] then decreased to 0.6 at infinite depth with an attenuation of 0.1.[81] The diffusion coefficients of solutes were calculated by the "diffcoeff" function in marelac (v2.1.11)[73] considering in-situ temperature and pressure and then corrected for tortuosity.[90] The boundary conditions were established in two ways: 1) Dissolved compounds were set to have constant concentrations at the seawater-sediment boundary; 2) Solid TOC and MnO_2 were set to have constant sedimentary influx. The R packages ReacTran (v1.4.3.1) were utilized to solve the model.[74]

Then, the model parameters were calibrated to fit the measured TOC, sulfate, ammonium, nitrate, nitrite, and dissolved oxygen concentrations using the differential evolution optimization method from the R package DEoptim (v2.2.6).[34] The deviation between model-predicted and measured profiles were evaluated by normalized root mean squared error (NRMSE):

$$\mathrm{NRMSE} = \frac{\sqrt{\frac{1}{n}\sum_{i=1}^{n}(C_i - \widehat{C}_i)^2}}{\max(C) - \min(C)} \quad \text{(Equation 8)}$$

where C_i is the measured compound concentration in sediment layer i and $\widehat{C}_i$ is the model-predicted compound concentration in sediment layer i.

For the reactions with generally recognized marker genes (Table S4), we further evaluated the agreement between predicted biogeochemical reaction rates and observed gene abundances in metagenomic data by calculating the normalized root mean square error (NRMSE) between standardized values. Both the predicted reaction rates (r) and observed gene abundances (g) were first standardized using z-score normalization:

$$r_{scaled} = \frac{r - \bar{r}}{s_r} \quad \text{(Equation 9)}$$

$$g_{scaled} = \frac{g - \bar{g}}{s_g} \quad \text{(Equation 10)}$$

where $\bar{r}$ and $\bar{g}$ represent the means, and s_r and s_g represent the standard deviations of predicted reaction rates and observed gene abundances, respectively. The NRMSE was then calculated as:

$$\mathrm{NRMSE} = \frac{\sqrt{\frac{1}{n}\sum_{i=1}^{n}\left(r_{scaled\_i} - g_{scaled\_i}\right)^2}}{\max(r_{scaled}) - \min(r_{scaled})} \quad \text{(Equation 11)}$$

where n is the number of data points, and $\max(r_{scaled}) - \min(r_{scaled})$ represents the range of the scaled reaction rates. This approach quantifies how well the relative patterns of predicted biogeochemical activity match the relative patterns of functional gene abundance, normalized by the range of predicted rates to provide a scale-independent assessment of model-data agreement.

The model parameters (Tables S5 and S6) were tuned to minimize the sum of NRMSEs by the differential evolution optimization approach.[34] After 1,000 iterations, the optimized parameters were used to produce the model estimates. We repeated the calibration

workflow 10 times at each site to evaluate the robustness of this strategy. To indicate the sediment microbial activities, we calculated the MCU values by summing the microbial reaction rates that were associated with organic carbon degradation in the 0-35 cm range of each sediment core, including aerobic respiration, dissimilatory Fe/Mn reduction, nitrate reduction to nitrite, denitrification from nitrite, dissimilatory nitrate reduction to ammonium (DNRA) from nitrite, and sulfate reduction (Figure 6A).

QUANTIFICATION AND STATISTICAL ANALYSIS

Statistical analyses and quantification in this work were performed in base R (v4.5.2)[46] and R package vegan (v2.6.4).[49] Non-parametric tests were used throughout the manuscript, unless noted otherwise, i.e. Spearman's rank correlation test and permANOVA test. For multiple comparisons, p-values were adjusted using the "FDR" method.[91] Relations between geochemical model predictions and topography were assessed using linear models. Statistical details, including statistical tests used, exact value of n (number of samples), and p-values can be found in corresponding figure legends and result context.